Doctoral Dissertation (Censored)

博士論文（要約）

Photo-induced charge transfer in $[Ar\text{-}N_2]^+$ and electron diffraction of CCl_3^+ by ion trap

（イオントラップによる$[Ar\text{-}N_2]^+$の光誘起電荷移動およびCCl_3^+の電子回折）

A Dissertation Submitted for the Degree of Doctor of Philosophy

December 2020

令和 2 年 12 月博士（理学）申請

Department of Chemistry, Graduate School of Science,

The University of Tokyo

東京大学大学院理学系研究科

化学専攻

Takahiro Suzuki

鈴木　貴裕

Doctoral Dissertation

博士論文

Photo-induced charge transfer in $[Ar\text{-}N_2]^+$ and electron diffraction of CCl_3^+ by ion trap

（イオントラップによる$[Ar\text{-}N_2]^+$の光誘起電荷移動およびCCl_3^+の電子回折）

A Dissertation Submitted for the Degree of Doctor of Philosophy

December 2020

令和 2 年 12 月博士（理学）申請

Department of Chemistry, Graduate School of Science,

The University of Tokyo

東京大学大学院理学系研究科

化学専攻

Takahiro Suzuki

鈴木貴裕

Abstract

When ion complexes $[A\text{-}B]^+$ are trapped in an ion trap, its photo-excitation will give us an opportunity to investigate a charge transfer reaction within the complex, leading to two different products, that is, $A + B^+$ and $A^+ + B$. In my thesis study, I investigate the mechanism of intermolecular charge transfer processes in $[Ar\text{-}N_2]^+$ induced by intense femtosecond near-IR laser fields by ion-trap time-of-flight mass spectrometry and show that non-adiabatic couplings among the potential energy curves of the electronic states play a crucial role in the charge transfer reactions, producing the product pairs of $Ar + N_2^+$ and $Ar^+ + N_2$.

On the other hand, it has been known that geometrical structures of molecular ions can be determined by electron diffraction measurements of molecular ions trapped in an ion trap and the distances between neighboring nuclei in highly symmetric large size clusters such as C_{60}^+ and Ru_{20}^- were estimated. However, it has been an extremely difficult task to determine geometrical structures of small-sized molecular ions by the ion-trap gas electron diffraction method because the density of the molecular ions in an ion trap could not be higher than 10^7 molecules/cm^3, which is comparable with the density of background gas species in a vacuum chamber. In my thesis study, I develop a trapped-ion electron diffraction apparatus for molecular ions and succeed in recording an electron diffraction pattern of CCl_3^+ generated by dissociative ionization of CCl_4 by decreasing sufficiently the background signals originating from the scattering electrons by residual gas and those from the back-scattered and secondary electrons from a Faraday cup. The optimized internuclear distances obtained by the least-squares analysis of the molecular scattering intensity were determined to be $r_{C\text{-}Cl}$ = 1.66(2) Å and $r_{Cl\text{-}Cl}$ = 2.87(2) Å, which are in good agreement with the previous theoretical values.

Chapter 1. General introduction..... 1

1.1 Ion trap..... 1

1.2 Ion trap time-of-flight mass spectrometry..... 5

1.3 Collision ion complex..... 6

1.4 Trapped ion electron diffraction..... 8

References..... 11

Chapter 2. Charge transfer in $[Ar\text{-}N_2]^+$ induced by near-IR femtosecond intense laser fields by ion-trap time-of-flight mass spectrometry..... 14

2.1 Introduction..... 14

2.2. Experimental setup..... 19

2.3. Results and discussion..... 24

2.3.1. Ion-trap mass spectroscopy..... 24

2.3.2. Photodissociation pathways..... 26

2.3.3. Adiabatic and non-adiabatic population transfer..... 28

2.3.4. Numerical simulations of adiabatic and non-adiabatic population transfer..... 30

2.3.5. Numerical simulations with intra-complex energy transfer..... 33

2.4. Conclusion..... 36

Appendix: Confirmation of one-photon transitions..... 37

References..... 41

Chapter 3. Determination of geometrical structure of CCl_3^+ by trapped-ion electron diffraction..... エラー! ブックマークが定義されていません。

3.1 Introduction ..... エラー! ブックマークが定義されていません。

3.2 Experimental setup ..... エラー! ブックマークが定義されていません。

3.2.1 Vacuum system ..... エラー! ブックマークが定義されていません。

3.2.2 Sample gas introduction system エラー! ブックマークが定義されていません。

3.2.3 Electron gun ..... エラー! ブックマークが定義されていません。

3.2.4 Ion trap ..... エラー! ブックマークが定義されていません。

3.2.5 Detection system ..... エラー! ブックマークが定義されていません。

3.2.6 Faraday cup ..... エラー! ブックマークが定義されていません。

3.2.7 Experimental procedure ..... エラー! ブックマークが定義されていません。

3.3 Results ..... エラー! ブックマークが定義されていません。

References ..... エラー! ブックマークが定義されていません。

Chapter 4. Summary and future perspective **57**

Charge transfer in $[Ar\text{-}N_2]^+$ induced by near-IR femtosecond intense laser fields by ion-trap time-of-flight mass spectrometry **57**

Determination of geometrical structure of CCl_3^+ by trapped-ion electron diffraction ... **58**

Acknowledgements **59**

Chapter 1. General introduction

1.1 Ion trap

Ion traps have played a very important role in the study of natural sciences. The density of ions is extremely low due to the Coulomb repulsion. In addition, since by-product ion species and neutral molecules are mixed with target ion species during ion generation, the experiment for using ions was extremely difficult. The ion trap, which was developed as a method to solve these problems, is a device that can trap charged particles in a vacuum chamber three-dimensionally using electromagnetic fields, and the ion trap is used for research on charged particles such as ions. There are mainly two types of ion traps. The first type is trapping charged particles using an electrostatic field and a static magnetic field, which is called a Penning trap[1] because it was devised by F. M. Penning in 1936. On the other hand, the second type is trapping charged particles by combining an

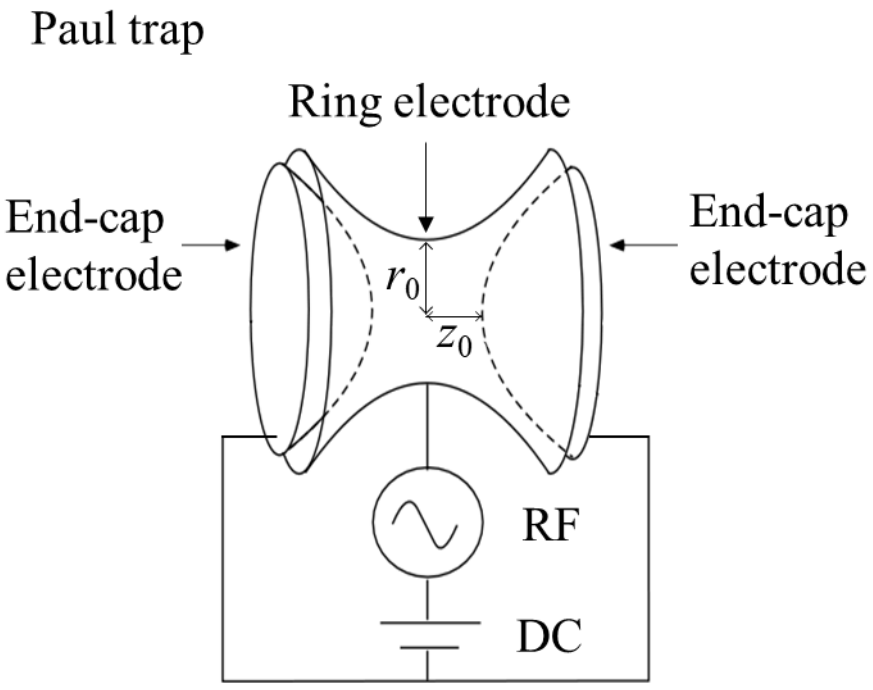

Figure 1.1 Electrodes structure of Paul trap.

electrostatic field and a high-frequency electric field, which was devised by W. Paul in 1953 and is called a Paul trap.[2] The Paul trap is also called a RF trap because radio frequency was used for the high-frequency electric field. Both ion traps are apparatuses that can trap and store charged particles mass-selectively for a long time. However, since the Penning trap uses a static magnetic field and the energy level of the trapped ions is split by the Zeeman effect, the Paul trap is generally used in quantum chemistry research.

The Paul trap[3-8] consists of two end-cap electrodes and a ring electrode. By applying voltages to the electrodes, quadrupole electric fields are generated in the ion trap. The ring electrode is located symmetrically between two end-cap electrodes as shown in Fig. 1.1 and ions are trapped in the central space surrounded by these three electrodes. The end-cap electrodes have hyperboloidal geometry and the ring electrode has an internal hyperboloidal surface. The radius of the ring electrode in the central plane is r_0 and the distance between the two end-cap electrodes is $2z_0$ as shown in Fig. 1.1. In the cylindrical coordinates, the equations for the cross-section of the electrodes are written as

$$\frac{r^2}{2z_0^2} - \frac{z^2}{z_0^2} = -1 \quad \text{(end-cap electrode)} \tag{1.1}$$

and

$$\frac{r^2}{r_0^2} - \frac{z^2}{r_0^2} = 1 \quad \text{(ring electrode)} \tag{1.2}$$

in which z is the axial coordinate, which is the axis of rotation of the ring electrodes, and r is the distance from the z-axis. In addition, r_0 and z_0 are related to each other as

$$r_0^2 = 2z_0^2, \tag{1.3}$$

so that the quadrupole potential is generated. In order to trap charged particles in the ion trap, a radio frequency voltage and a direct voltage are applied to the ring electrode. The applied voltage ϕ_0 is given by a RF voltage V with the angular frequency Ω and the direct voltage U as

$$\phi_0 = U + V\cos\Omega t. \tag{1.4}$$

The quadrupole potential in the ion trap is given by

$$\phi(r, z) = \frac{\phi_0}{2r_0^2}(r^2 - 2z^2). \tag{1.5}$$

By differentiation of the Eq. (1.5), the amplitudes of the electric field are given by

$$E_z = -\frac{\partial\phi(r, z)}{\partial z} = 2(U + V\cos\Omega t)\frac{z}{r_0^2} \tag{1.6}$$

$$E_r = -\frac{\partial\phi(r, z)}{\partial r} = -(U + V\cos\Omega t)\frac{r}{r_0^2}. \tag{1.7}$$

The equations of motion of a charged particle whose mass-to-charge ratio is m/e in the quadrupole potential field of the ion trap are

$$\frac{d^2z}{dt^2} = 2(U + V\cos\Omega t)\frac{ez}{mr_0^2} \tag{1.8}$$

and

$$\frac{d^2r}{dt^2} = -(U + V\cos\Omega t)\frac{er}{mr_0^2}. \tag{1.9}$$

Because the valuable in Eq. (1.8) is only z and that in Eq. (1.9) is only r, the motion in the z-axis direction and the motion in the plane perpendicular to the z-axis are mutually independent. By using dimensionless constants

$$\tau = \frac{\Omega t}{2}, \tag{1.10}$$

$$a_z = -2a_r = 2\frac{eU}{mr_0^2\Omega^2}, \tag{1.11}$$

and

$$q_z = -2q_r = 2\frac{eV}{mr_0^2\Omega^2}, \tag{1.12}$$

the Eqs. (1.8) and (1.9) can be written as the Mathieu differential equation,

$$\frac{d^2u}{dt^2} - (a_u + 2q_u\cos 2\tau) = 0, \tag{1.14}$$

in which u represents either z or r. The solution of Eq. (1.14) is given by

$$u = Ae^{\mu\tau}\sum_{n=-\infty}^{\infty} C_{2n}e^{i2n\tau} + Be^{-\mu\tau}\sum_{n=-\infty}^{\infty} C_{2n}e^{-i2n\tau} \tag{1.15}$$

in which the quantities μ and C_{2n} are functions of a_u and q_u. Therefore, the motion of a charged particle in the ion trap is determined by the values of a_u and q_u. Equation (1.15) has two different types of solutions. In one of the two solutions, the amplitude of the oscillation motion of a charged particle builds up exponentially and the charged particle is not stably trapped in the ion trap. In the other solution, the charged particle can be trapped stably in the ion trap when the variables a_u and q_u are in the region surrounded by the curves represented by

$$a_u = -\frac{1}{2}q_u^2 + \frac{7}{128}q_u^4 - \frac{29}{2304}q_u^6 + \frac{68687}{18874368}q_u^8 + O(q_u^{10}) \tag{1.16}$$

and

$$a_u = 1 - q_u - \frac{1}{8}q_u^2 + \frac{1}{64}q_u^3 - \frac{1}{1536}q_u^4 + \frac{11}{35864}q_u^5 + O(q_u^6). \tag{1.17}$$

The stable region for the ion trapping is shown in Fig. 1.2, which is referred to as a stability diagram. Once the applied voltage U, V, and the frequency of the RF voltage Ω are given, the range of mass-to-charge ratio of charged particles that can be stably trapped in the ion trap can be determined by the

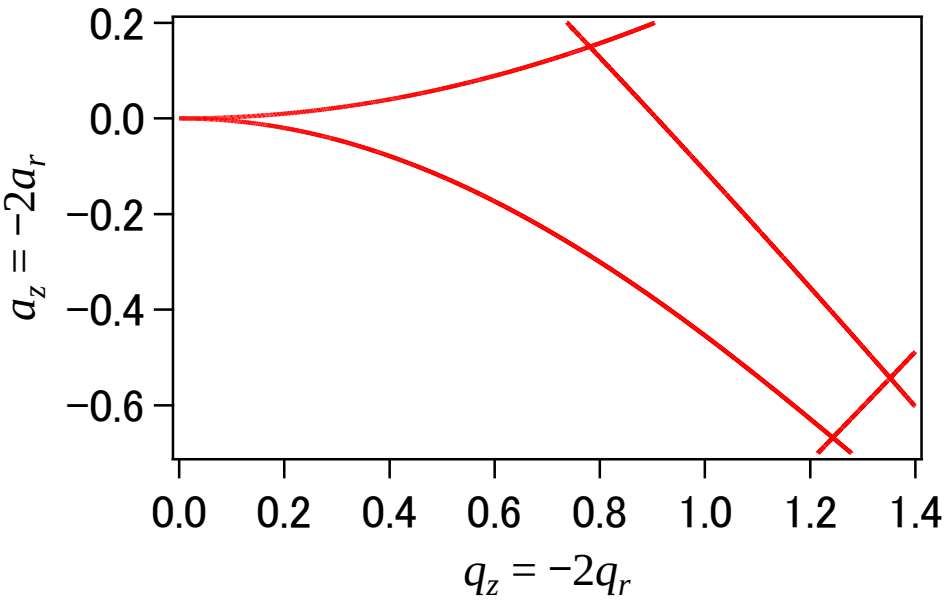

Figure 1.2 Stability diagram in the (a_u,q_u) space for the ion trap. Charged particles can be trapped stably in the ion trap when the variables a_u and q_u are in the region surrounded by the four curves.

stability diagram. By varying properly the applied voltages and the RF frequency, the range of mass-to-charge ratios of trapped charged particles is adjusted. By widening this range, we can increase the number of different ion species that can be trapped at the same time, and, by narrowing this range, we can trap single ion species mass-selectively.

1.2 Ion trap time-of-flight mass spectrometry

By applying a pulsed high voltage to the end-cap electrode, the trapped ions can be accelerated and extracted from the ion trap into the flight tube. Because the velocity of ions in a grounded flight tube depends on their mass-to-charge ratio, the ion species are spatially separated by their mass-to-charge ratio, so that they reach the detector placed at the end of the flight tube at the different timings and their mass spectrum is recorded. By this method called an ion-trap time-of-flight mass spectrometry, we can perform mass spectrometry of fragment ion species generated from molecules and molecular ions by photoirradiation. In the previous studies,[7,9-28] it was shown that even fragment ion species with an extremely small amount of production could be detected by the accumulation of ions using an ion trap. In addition, it was reported that ion complexes[7,9,15-19] and fragment ion species,[7,9-13,16,18] which were generated by the collision process between trapped ions and neutral molecules, could be detected. Furthermore, the chemical reactions induced by collision processes among ions and molecules were also investigated.[7,9-13,15-19] It was also shown that, by increasing the sample density of the trapped ions using an ion trap, the vibration spectrum of ion species with a small amount of production such as complex ions were measured and its structural analysis were perforemed.[29,30]

It is also possible to trap only target ion species with a specific mass-to-charge ratio exclusively by adjusting the RF voltage and the direct voltage applied to the ring electrodes. Photodissociation of mass-selective ion species trapped in the ion trap was induced by laser

irradiation,[25-28] and the photodissociation processes starting from ion species were investigated. However, when there are ion species having small differences in the mass-to-charge ratio with respect to the target ion species to be measured, it becomes sometimes difficult to trap only the target ion species exclusively even when the magnitudes of the RF voltage and the direct voltage are adjusted. In order to overcome this difficulty, a method called stored waveform inverse Fourier transform (SWIFT)[30] was introduced. The translational motion of the ions trapped in the ion trap can be approximately regarded as a harmonic oscillating motion. Therefore, by applying an alternating current voltage, whose frequency is in resonance with the frequency of the harmonic oscillation of the trapped ions, to the end-cap electrodes, we can amplify largely the amplitude of harmonic oscillation of the trapped ions so that they escape from the ion trap. In the SWIFT method, we apply alternating current voltages containing multiple frequency components except the oscillation frequency of the ion species we hope to trap and achieve the exclusive trapping of the specific ion species. By the SWIFT method, we can raise the mass selectivity of the ion trap significantly while keeping the sample density of the target ion species.[19-24]

1.3 Collision ion complex

The advantage of ion traps is the efficient storage of collision ion complexes and cluster ions. In the previous studies,[32-34] collision ion complexes were generated by the ionization of collision molecular complexes, which were generated through the expansion of high-pressure gases into vacuum and by collisions between neutral molecules and ions through the ion beam irradiation to neutral molecules. However, the number of collisions is in general very small, and consequently, the density of the collision ion complexes cannot be sufficiently high. Furthermore, because ion complexes other than the target ion complex and the monomer ions that do not form complexes coexist, experiment using the target ion complex exclusively has been a difficult task. However, this difficulty

can be overcome using an ion trap. By trapping ions in a confined space for a long time using an ion trap and introducing neutral molecules into the ion trap, it becomes possible to increase the number of collisions between ions and molecules generate efficiently collision ion complexes. Furthermore, by combining the SWIFT method, monomer ions and ion complexes other than the target ion complex species can be eliminated, resulting in the efficient mass-selective trapping of the target collision ion complexes.[19]

The intermolecular reaction induced by the collision process of molecules proceeds via the formation of a transition collision complex. However, it is difficult to investigate the intermolecular reaction induced by the collision process because the formation of the transition collision complex and the successive reaction proceed in an extremely short period of time. Therefore, a weekly bound collision complexes has been adopted as a model system mimicking the transition state of a collision-induced chemical reaction.[35-39] In the previous studies,[36,37] in order to elucidate the intermolecular charge transfer reaction,

$$Ar^+(^2P_{3/2}) + N_2(X\ ^1\Sigma_g^+)\ (v) \rightarrow Ar(^1S) + N_2^+(X\ ^2\Sigma_g^+)\ (v_{ion}), \quad (1)$$

and its reverse reaction,

$$Ar(^1S) + N_2^+(X\ ^2\Sigma_g^+)\ (v_{ion}) \rightarrow Ar^+(^2P_{3/2}) + N_2(X\ ^1\Sigma_g^+)\ (v), \quad (2)$$

the photodisociation processes of $[Ar\text{-}N_2]^+$ ion species induced by ultraviolet (UV) and visible laser pulses were investigated. It was shown that the photodissociation of $[Ar\text{-}N_2]^+$ ions proceeds through the following two pathways:

$$[Ar\text{-}N_2]^+ + h\nu \rightarrow Ar(^1S) + N_2^+(X\ ^2\Sigma_g^+)\ (v_{ion}), \quad (3)$$

and

$$[Ar\text{-}N_2]^+ + h\nu \rightarrow Ar^+(^2P_{3/2}) + N_2(X\ ^1\Sigma_g^+)\ (v). \quad (4)$$

It was also reported[36] that, when $[Ar\text{-}N_2]^+$ was irradiated with Ar-ion laser light at 458 nm, the vibrationally excited states of N_2 (v = 0–4) and N_2^+ (v_{ion} = 0–5) were created. In order to clarify the

charge transfer reaction, it would be desirable to induce photodissociation by the laser pulses having the longer wavelength than the previous studies so that the photodissociation process is less complicated by the reduction of the number of the vibrationally and electronically excited states involved in the photodissciation process. In Chapter 2 of the present thesis, mass-selective $[Ar\text{-}N_2]^+$ ions were generated efficiently by using an ion trap and photodissciation of $[Ar\text{-}N_2]^+$ ions was induced by the irradiation of the near-IR (~800 nm) laser pulses. The photodissociation mechanism was investigated based on the yield ratios of the fragment ion species of Ar^+ and N_2^+ were measured by ion trap time-of-flight mass spectrometry.

1.4 Trapped ion electron diffraction

The trapped-ion electron diffraction (TIED) method is an experimental method in which an electron beam accelerated at high speed is scattered by mass-selectively trapped ions to determine their geometrical structure from a recorded gas electron diffraction pattern. Previously, the geometrical structure of cluster ions has been studied by the TIED method.[40-47] In the gas electron diffraction experiment on gaseous molecules, the electron diffraction pattern is recorded, from which the internuclear distances of the molecular species are determined with the precision as high as 0.01 Å. Indeed, the geometrical structures of a large number of neutral molecular species have been determined with high precision by the gas electron diffraction method. However, when it comes to molecular ion species, the determination of their geometrical structures by gas electron diffraction is not an easy task because the sample density of molecular ions could not be sufficiently high due to their Coulomb repulsion. Even when the sample density can be increased by trapping ions using the ion trap, the sample density of the ions is much lower than that of neutral molecules. However, if molecular ions are trapped in the ion trap and the electron diffraction signals are accumulated for a long period of time, the electron diffraction pattern of the molecular ions can be recorded, from which

the geometrical structure of molecular ions can be determined with high precision. Therefore, it can be said that the TIED method is a promising experimental method for the determination of the geometrical of molecular ions. Indeed, it was reported that cluster ions were trapped in the ion trap for as long as 45 seconds and were irradiated with a continuous electron beam.[40] However, due to the low signal intensities, it is prerequisite to reduce the background signals as much as possible in the TIED measurements. In the pioneering study conducted by Parks et al.[40-47], they achieved a ratio of the number of electrons in the background signals (n_b) with respect to the number of incident electrons (n_i) as low as $n_b/n_i = 1.6\times10^{-8}$. In a series of the TIED studies, they performed TIED measurements of cluster ions such as C_{60}^+ ions,[40] Ag_{55}^+ ions,[42,43] and Ru_{20}^- ions,[47] which have a large electron scattering cross section and a periodic structure. However, TIED measurements of small-sized molecular ions have not been reported so far because of their small electron scattering cross section, which is smaller than those of the cluster ions by two orders of magnitude. In order to record an electron diffraction pattern of such small-sized molecular ions by the TIED measurements, it is necessary to reduce further the ratio of n_b/n_i.

In Chapter 3 of the present thesis, in order to reduce the background signals as much as possible, I developed an experimental setup for the TIED measurements shown in Fig. 1.3, conducted TIED measurements for CCl_3^+, and determined its geometrical structure from the analysis of a recorded diffraction pattern. In the experimental apparatus a position sensitive detector with a central hole was installed as shown in Fig. 1.3 and a Faraday cup was placed behind the detector, so that the background signals originating from electrons reflected from the Faraday cup and secondary electrons generated at the Faraday cup create could be detected. Furthermore, in order to reduce the background signals originating from the electrons scattered by the residual gases in the vacuum chamber the ion trap electrodes were cooled to 77 K with liquid nitrogen. The significant reduction of the background

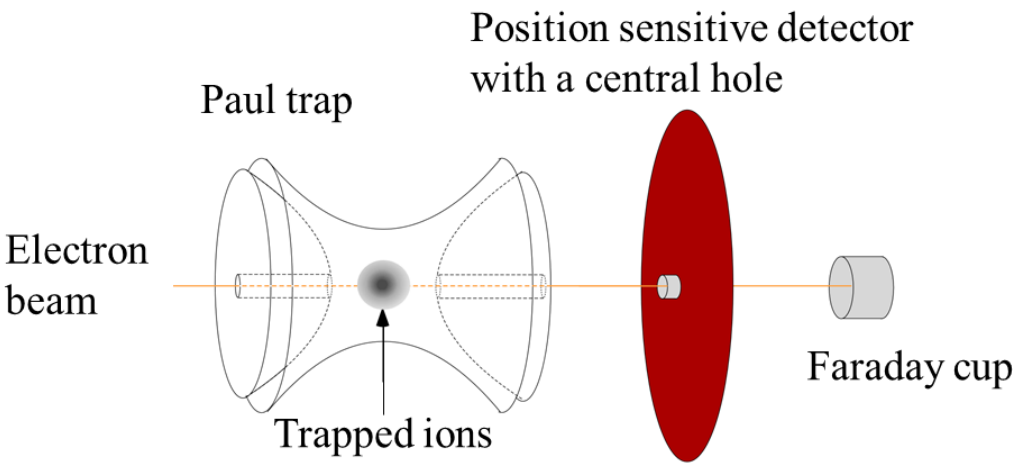

Figure 1.3 Schematics of experimental setup for TIED.

signals achieved in this study enabled the first measurements of a gas electron diffraction pattern of small polyatomic molecular species by the TIED method.

References

[1] F. M. Penning, *Physica*, **3**, 873 (1936).

[2] W. Paul and H. Steinwedel, *Z. Naturforsch* **8a**, 448 (1953).

[3] R. F. Wuerker, H. Shelton, and R. V. Langmuir, *J. Appl. Phys*. **30**, 342 (1959).

[4] W. Paul, *Rev. Mod. Phys*. **62**, 531 (1990).

[5] H. Dehmelt, *Rev. Mod. Phys.* **62**, 525 (1990).

[6] W. Paul, *Angew. Chem. Int. Ed. Engl*. **29**, 739 (1990) .

[7] R. E. March, *J. Mass Spectrom*. **32**,351 (1997).

[8] R. E. March, *Mass Spectrom.Rev.* **28**, 961 (2009).

[9] M. A. Armitage, J. E. Fulford, D.-N.-Hoa, R. J. Hughes, and R. E. March, *Can. J. Chem*. **57**, 2108 (1979).

[10] J. N. Louris, R. G. Cooks, J. E. P. Syka, P. E. Kelley, G. C. Stafford, and J. F. J. Todd, *Anal. Chem.* **59**, 1677 (1987).

[11] J .N. Louris, J.W. Amy, T.Y. Ridley, and R.G. Cooks, *Int. J. Mass Spectrom. Ion Processes*, **88**, 97 (1989).

[12] J. N.L. Jennifer, S. B.-Lustig, R. G. Cooks, G. L. Glish, G. J. v. Berkel, and S. A. McLuckey, *Int. J. Mass Spectrom.* **96**, 117 (1990).

[13] J. F. J. Todd, *Mass Spectrom. Rev*. **10**, 3 (1991).

[14] J. C. Schwartz, J. E. P. Syka, and I. Jardine, *J. Am. Soc. Mass Spectrom*. **2**, 198 (1991).

[15] R. E. Kaiser, R. G. Cooks, G. C. Stafford, J. E.P. Syka, and P. H. Hemberger, *Int. J. Mass Spectrom. Ion Processes*, **106**, 79 (1991).

[16] R. E. March, *Int. J. Mass Spectrom. Ion Processes* **118/119**, 71 (1992).

[17] J. D. Williams and R. G. Cooks, *Rapid Commun. Mass Spectrom.* **6**, 524 (1992).

[18] S. M. Michael, B. M. Chien, and D. M. Lubman, *Anal. Chem.* **65**, 2614 (1993).

[19] R. K. Julian and R. G. Cooks, *Anal. Chem.* **65**, 1827 (1993).

[20] A. Colorado, J. X. Shen, V. H. Vartanian, and J. Brodbelt, *Anal. Chem*. **68**, 4033 (1996).

[21] R. Korner, M. Wilrn, K. Morand, M. Schubert, and Matthias Mann, *J. Am. Soc. Mass Spectrom*, **7**, 150 (1996).

[22] V. M. Doroshenko and R. J. Cotter, *Rapid Commun. Mass Spectrom.* **10**, 65 (1996).

[23] L. He, J.-T. Wu, S. Parus, and D. M. Lubman, *Rapid Commun. Mass Spectrom.* **11**, 1739 (1997).

[24] R. E. March, *Rapid Commun. Mass Spectrom.* **12**, 1543 (1998).

[25] V. M. Doroshenko and R. J. Cotter, *J. Mass Spectrom*, **33**, 305 (1998).

[26] A. N. Krutchinsky, M. Kalkum, and B. T. Chait, *Anal. Chem.* **73**, 5066 (2001).

[27] K. Kato and K. Yamanouchi, *Chem. Phys. Lett.* **397**, 237 (2004).

[28] T. Yamazaki, Y. Watanabe, R. Kanya, and K. Yamanouchi, *J. Chem. Phys.* **144**, 024313 (2016).

[29] D. W. Boo and Y. T. Lee, *J. Chem. Phys.* **103**, 514 (1995).

[30] M. Okumura, L. I. Yeh, and Y. T. Lee, *J. Chem. Phys.* **83**, 7 (1985).

[31] S. Guan and A. G. Marshall, *Int. J. Mass Spectrom. Ion Processes* **157/158**, 5 (1996).

[32] E. Teloy and D. Gerlich, *Chem. Phys.* **4**, 417 (1974).

[33] S. A. Nizkorodov, J. P. Maier, and E. J. Bieske, *J. Chem. Phys.* **103**, 1297 (1995).

[34] S. A. Nizkorodov, O. Dopfer, M. Meuwly, J. P. Maier, and E. J. Bieske, *J. Chem. Phys.* **105**, 1770 (1996).

[35] H. Masuhara and N. Mataga, *Acc. Chem. Res.* **14**, 312 (1981).

[36] H.-S. Kim and M. T. Bowers, *J. Chem. Phys.* **93**, 1158 (1990).

[37] T. F. Magnera and J. Michl, *Chem. Phys. Lett.* **192**, 99 (1992).

[38] K. F. Willey, C. S. Yeh, D. L. Robbins, and A. Duncan, *J. Chem. Phys*. **96**, 9106 (1992).

[39] Y. C. Cheng, J. Chen, L. N. Ding, T. H. Wong, P. D. Kleiber, and D. -K. Liu, *J. Chem. Phys*. **104**, 6452 (1996).

[40] M. M.-Borst, D. B. Cameron, M. Rokni, and J. H. Parks, *Phys. Rev. A* **59**, R3162 (1999).

[41] S. Krückeberg, D. Schooss, M. M.-Borst, and J. H. Parks, *Phys. Rev. Lett*, **85**, 4494 (2000).

[42] D. Schooss, M. N. Blom, J. H. Parks, B. v. Issendorff, H. Haberland, and M. M. Kappes, *Nano Lett.* **5**, 1972 (2005).

[43] X. Xing, R. M. Danell, I. L. Garzón, K. Michaelian, M. N. Blom, M. M. Burns, and J. H. Parks, *Phys. Rev. B*, **72**, 081405 (2005).

[44] X. Xing, B. Yoon, U. Landman, and J. H. Parks, *Phys. Rev. B*, **74**, 165423 (2006).

[45] M. P. Johansson, A. Lechtken, D. Schooss, M. M. Kapppes, and F. Furche, *Phys. Rev. A*, **77**, 053202 (2008).

[46] D. Schooss, P. Weis, O. Hampe, and M. M. Kappes, *Phil. Trans. R. Soc. A* **368**, 1211 (2010).

[47] E. Waldt, A.-S. Hehn, R. Ahlrichs, M. M. Kappes, *J. Chem. Phys.* **142**, 024319 (2015).

Chapter 2. Charge transfer in $[Ar\text{-}N_2]^+$ induced by near-IR femtosecond intense laser fields by ion-trap time-of-flight mass spectrometry

2.1 Introduction

In unimolecular and bimolecular reactions, non-adiabatic transitions at avoided crossings or conical intersections among the potential energy surfaces play a decisive role, and it has been a central issue to investigate how the non-adiabatic transitions affect the state-selectivity of the reactions. In collisional intermolecular charge transfer reactions, such as $A + B^+ \rightarrow A^+ + B$, the state distributions of products are determined by the non-adiabatic transitions between the potential energy surface leading to the dissociation into $A + B^+$ and that leading to the dissociation into $A^+ + B$. Among such collisional reactions, the reaction,

$$Ar^+(^2P_{3/2}) + N_2(X\ ^1\Sigma_g^+)\ (v) \rightarrow Ar(^1S) + N_2^+(X\ ^2\Sigma_g^+)\ (v_{ion}), \tag{2.1}$$

and its reverse reaction,

$$Ar(^1S) + N_2^+(X\ ^2\Sigma_g^+)\ (v_{ion}) \rightarrow Ar^+(^2P_{3/2}) + N_2(X\ ^1\Sigma_g^+)\ (v), \tag{2.2}$$

have been regarded as benchmark chemical reactions that have characteristic features of collisional intermolecular charge transfer reactions, where v and v_{ion} are the vibrational quantum numbers of N_2 and N_2^+, respectively.

In order to investigate the collisional intermolecular charge transfer reactions, Eqs. (2.1) and (2.2), we need to know the interaction potentials between the reactants. By high-resolution infrared spectroscopy,[1,2] it was confirmed that the equilibrium geometrical structure of this complex ion, $[Ar\text{-}N_2]^+$, in the electronic ground state is linear, that is, Ar and two N nuclei of the N_2 moiety are located on the same straight line. By *ab initio* MO calculations,[2,3] it was also shown that the equilibrium geometrical structure of this complex ion in the electronic ground state is linear and that the top of the barrier for the internal rotation of the N_2 moiety, whose height is of the order of 1.0 eV, is located at

the geometrical structure in which the N-N axis is perpendicular to the straight-line connecting Ar and the center of mass of the N_2 moiety.

The dissociation energy, D_0, of the electronic ground state of $[Ar\text{-}N_2]^+$, defined as the energy of the dissociation limit of "$Ar(^1S) + N_2^+(X\ ^2\Sigma_g^+)$" measured from the vibrational ground state, has been determined experimentally by electron impact ionization,[4] thermochemical measurements,[5,6] collision induced dissociation,[7,8] and dissociative ionization,[9,10] and all the experimental data are in the range between 0.9 and 1.2 eV. The origin of this relatively large dissociation energy was interpreted theoretically as the stabilization achieved by nearly perfect charge delocalization,[3] expressed as the superposition of the two resonance structures, "$Ar^+\cdots N_2$" and "$Ar\cdots N_2^+$."

It has been known that the electronic states of $[Ar\text{-}N_2]^+$ can be characterized by the projection Ω of the electronic angular momentum on the axis connecting Ar and the center of mass of the N_2 moiety.[11,12] In the electronic ground state, the projection quantum number is $\Omega = 1/2$. The potential energy curves of the first and second electronically excited states having respectively $\Omega = 3/2$ and 1/2 have the same dissociation limit of "$Ar^+(^2P_{3/2}) + N_2(X\ ^1\Sigma_g^+)$" and exhibit similar shape with a shallow bound well. The next higher lying electronic state having $\Omega = 1/2$ has the dissociation limit of "$Ar^+(^2P_{1/2}) + N_2(X\ ^1\Sigma_g^+)$" and exhibit a repulsive character.

In Eq. (2.1), the nuclear wave packet on the potential curve of the first electronically excited state, approaching the small R region from $R \sim \infty$, is transferred to the electronic ground state of $Ar(^1S)\cdots N_2^+(X\ ^2\Sigma_g^+)$ via the formation of the collision complex, followed by dissociation into $Ar(^1S) + N_2^+(X\ ^2\Sigma_g^+)$. Previous experimental studies, conducted by the flow method,[13–19] the collision cell method,[20–24] and the crossed beam method,[21,25–33] as well as previous theoretical studies[11,12,32,34–39] revealed that the state-to-state cross sections of the charge transfer reactions, the reactions, Eqs. (2.1) and (2.2), exhibit characteristic state-selectivities and the cross sections vary sensitively on the collision-energy. For example, N_2^+ ($v_{ion} = 1$) is the dominant product in the reaction Eq. (2.1) at the

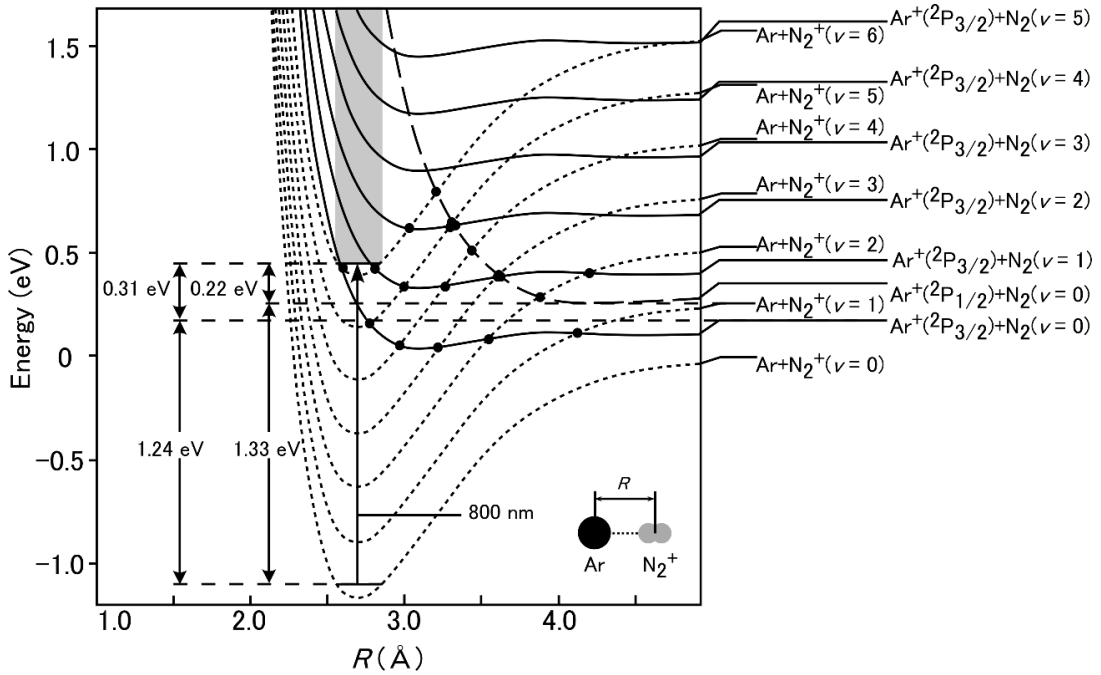

Figure 2.1. The schematic of vibronic potential energy curves of the $[Ar\text{-}N_2]^+$ ion in the linear geometry, drawn based on Ref. 12, as a function of *R*.

low collision energies below 4.1 eV[15] even though the production of N_2^+ ($v_{ion} = 0$) is more favorable energetically.

The low-lying potential energy curves of $[Ar\text{-}N_2]^+$ with $\Omega = 1/2$ having different vibrational quantum numbers of N_2 and N_2^+ moieties are shown in Fig. 2.1, which is a retrace of the corresponding figure reported by Candori *et al.*[12] In Fig. 2.1, the second electronically excited state with $\Omega = 3/2$ is not drawn. This is because Ω is expected to be conserved in the collisional reaction as long as the linear geometrical structure is kept in the course of the reaction. Indeed, in the complex domain, no charge transfer is expected to occur between $Ar^+(^2P_{3/2})\cdots N_2(X\ ^1\Sigma^+_g)$ [$\Omega = 3/2$] and $Ar(^1S)\cdots N_2^+(X\ ^2\Sigma_g^+)$ [$\Omega = 1/2$] at their crossing points.

On the other hand, the crossings among the potential energy curves having $\Omega = 1/2$ and different vibrational quantum numbers in the N_2 moiety are avoided because of the vibronic coupling. There are two possible pathways at each of the avoided crossings, that is, (i) the adiabatic pathway through which the vibrational quantum number in the N_2 moiety changes associated with the charge

transfer between the Ar and N_2 moieties and (ii) the non-adiabatic pathway through which neither the change in the vibrational quantum number in the nitrogen molecular moiety or the charge exchange between the Ar and N_2 moieties occurs.

In order to examine the mechanism of the bifurcation into the adiabatic and nonadiabatic pathways at the respective avoided crossings occurring in the structural domain of a transient collision complex $[Ar\cdots N_2]^+$, it is worthy to start the collisional reactions, Eqs. (2.1) and (2.2), from the collisional complex by the photoexcitation of a weakly bound $[Ar\text{-}N_2]^+$ complex in the electronic ground state and investigate the bifurcation processes occurring at the potential energy curve crossings located in the Franck-Condon region within the $\Omega = 1/2$ manifold. Considering that the optical transition from $Ar(^1S)\cdots N_2^+(X\ ^2\Sigma_g^+)$ to $Ar^+(^2P_{3/2})\cdots N_2(X\ ^1\Sigma_g^+)$ promotes an intra-complex charge transfer to a large extent, the transition moment for the optical transition is expected to be along the axis connecting the Ar and N_2 moieties, which means that the selection rule for the optical transition is $\Delta\Omega = 0$. Therefore, $Ar^+(^2P_{3/2})\cdots N_2(X\ ^1\Sigma_g^+)$ [$\Omega = 1/2$] is expected to be created almost exclusively upon the photoexcitation of $Ar(^1S)\cdots N_2^+(X\ ^2\Sigma_g^+)$ [$\Omega = 1/2$]. It is possible that $Ar^+(^2P_{3/2})\cdots N_2(X\ ^1\Sigma_g^+)$ [$\Omega = 3/2$] is created upon the photoexcitation according to the selection rule of $\Delta\Omega = 1$, but the probability of this perpendicular transition is considered to be significantly small. If $Ar^+(^2P_{3/2})\cdots N_2(X\ ^1\Sigma_g^+)$ [$\Omega = 3/2$] is created, it is decomposed into $Ar^+(^2P_{3/2}) + N_2(X\ ^1\Sigma_g^+)$ exclusively because this electronic state with $\Omega = 3/2$ cannot interact with the electronic states with $\Omega = 1/2$, via which the intra-complex charge transfer can proceed.

In the previous experiments[40,41] on the photodissociation of mass-selected $[Ar\text{-}N_2]^+$, $[Ar\text{-}N_2]^+$ was irradiated with Ar-ion laser light at 357, 458, 488, 514, and 590 nm[40] and with nanosecond laser pulses in the range between 270 and 650 nm,[41] and it was shown that the photodissociation proceeds through the following two pathways;

$$[Ar\text{-}N_2]^+ + h\nu \rightarrow Ar(^1S) + N_2^+(X\ ^2\Sigma_g^+)\ (v_{ion}) \tag{2.3}$$

and

$$[\mathrm{Ar\text{-}N_2}]^+ + h\nu \rightarrow \mathrm{Ar}^+(^2\mathrm{P}_{3/2}) + \mathrm{N_2}(\mathrm{X}\ ^1\Sigma_g^+)\ (v). \tag{2.4}$$

When $[\mathrm{Ar\text{-}N_2}]^+$ in the electronic ground state is irradiated with UV and visible light, it is excited to the first electronically excited states, $\mathrm{Ar}^+(^2\mathrm{P}_{3/2})\cdots\mathrm{N_2}(\mathrm{X}^1\Sigma^+_g)$, which is correlated asymptotically to the dissociation limit of $\mathrm{Ar}^+(^2\mathrm{P}_{3/2}) + \mathrm{N_2}(\mathrm{X}^1\Sigma_g^+)$. After the photoexcitation, the decomposition proceeds through the following two possible channels, that is, the charge transfer channel,

$$\begin{aligned}\mathrm{Ar}^+(^2\mathrm{P}_{3/2})\cdots\mathrm{N_2}(\mathrm{X}\ ^1\Sigma^+_g) &\rightarrow \mathrm{Ar}(^1\mathrm{S})\cdots\mathrm{N_2}^+(\mathrm{X}\ ^2\Sigma_g^+)\\ &\rightarrow \mathrm{Ar}(^1\mathrm{S}) + \mathrm{N_2}^+(\mathrm{X}\ ^2\Sigma_g^+),\end{aligned} \tag{2.5}$$

and the channel with no charge transfer,

$$\mathrm{Ar}^+(^2\mathrm{P}_{3/2})\cdots\mathrm{N_2}(\mathrm{X}\ ^1\Sigma^+_g) \rightarrow \mathrm{Ar}^+(^2\mathrm{P}_{3/2}) + \mathrm{N_2}(\mathrm{X}\ ^1\Sigma^+_g). \tag{2.6}$$

It was reported[40,41] that the ratio γ of the yield of the intra-complex charge transfer channel, Eq. (2.5), with respect to the sum of the yield of Eq. (2.5) and that of Eq. (2.6) defined as

$$\gamma = \frac{I(\mathrm{N_2^+})}{I(\mathrm{Ar^+}) + I(\mathrm{N_2^+})}, \tag{2.7}$$

was found to be $\gamma \sim 0.2$ in the entire wavelength rage between 270 and 650 nm. It was also reported[40] that, when $[\mathrm{Ar\text{-}N_2}]^+$ was irradiated with Ar-ion laser light at 458 nm, the vibrationally excited states of $\mathrm{N_2}$ (v = 0–4) and $\mathrm{N_2}^+$ (v_{ion} = 0–5) were created. If the Franck-Condon principle of the $\mathrm{N_2}$ moiety[42] is taken into account, it is expected that $[\mathrm{Ar\text{-}N_2}]^+$ is prepared first in the bound part of the potential energy curve correlated to the dissociation limit of "$\mathrm{Ar}^+(^2\mathrm{P}_{3/2}) + \mathrm{N_2}(\mathrm{X}\ ^1\Sigma_g^+)$ (v = 0)." Therefore, the production of the vibrationally excited $\mathrm{N_2}$ and $\mathrm{N_2}^+$ means that the $\mathrm{N_2}$ moiety can be vibrationally excited through the adiabatic population transfer in the course of the dissociation. Because the vibrational excitation can proceed at the respective avoided crossings, the extent of the vibrational excitation is determined by the probabilities of the bifurcation at the respective avoided crossings. It is expected that the bifurcation processes will become simpler if the wavelength of the excitation laser

pulses is longer, that is, the excess energy of the photoexcited $[Ar\text{-}N_2]^+$ is lower, so that the number of the avoided crossings that photoexcited $[Ar\text{-}N_2]^+$ can access becomes smaller.

In the present study, in order to investigate the excess-energy dependence of the photodissociation reaction of $[Ar\text{-}N_2]^+$, $[Ar\text{-}N_2]^+$ ions prepared selectively in the Paul-type quadrupole ion trap are irradiated with femtosecond near-IR laser pulses (λ = 800 nm, Δt = 40 fs, I = 1.9–3.1×10^{14} W/cm^2) and the resultant fragment ion species, i.e. Ar^+ and N_2^+, are detected by time-of-flight mass spectrometry. Based on the yield ratio γ obtained in the present study at 800 nm and the yield ratios obtained before by the irradiation with the shorter wavelength laser light, the mechanism of the intra-complex charge transfer proceeding in the course of the photodissociation reactions, Eqs. (2.5) and (2.6), are investigated.

2.2. Experimental setup

Figure 2.2(a) shows the schematic of the experimental setup.[43,44] The apparatus is composed of a molecular beam source, a Paul-type quadrupole ion trap, and a time-of-flight (TOF) mass spectrometer. A gas mixture of Ar and N_2 (1:1) is introduced into a vacuum chamber through a pulsed nozzle whose orifice diameter is 0.8 mm at the stagnation pressure of 0.5 MPa. The resultant molecular beam is skimmed by a skimmer whose orifice diameter is 0.5 mm and the skimmed molecular beam is introduced into the ion trap.

The skimmed molecular beam is irradiated with femtosecond intense laser pulses (λ = 800 nm, Δt = 40–400 fs, I = 1.9–3.1×10^{14} W/cm^2) so that Ar^+ and N_2^+ are generated at the central position of the ion trap by the photoionization of the sample gas mixture. The voltage of the radio frequency (RF) wave whose frequency is 500 kHz (hereafter called trap-RF) is applied to the central ring electrode of the ion trap so that the generated ions are stored in the ion trap. In the ion trap, through

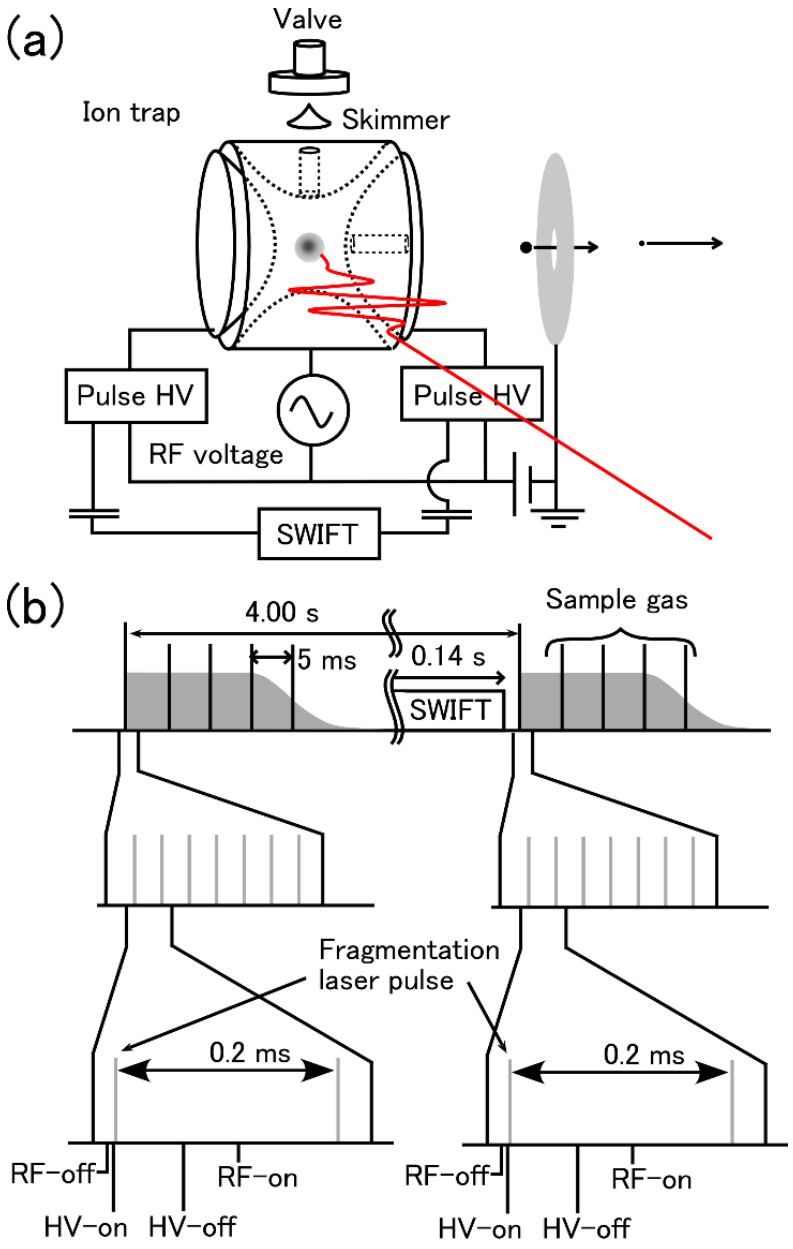

Figure 2.2. The schematic of the experimental setups: (a) the apparatus for ion-trap time-of-flight mass spectrometry, (b) a timing chart for the present measurements.

the collisions of the stored ions with neutral Ar and N_2, complex ions, $[Ar\text{-}N_2]^+$, are formed, and then, $[Ar\text{-}N_2]^+$ ions are exclusively stored in the ion trap by a method called stored waveform inverse Fourier transform (SWIFT).[45] In the SWIFT method, all ions except target ion species are removed from the ion trap by additional RF (hereafter called SWIFT-RF) voltage outputs of an arbitrary function

generator (Tektronix AFG3022B) applied to the two end-cap electrodes of the ion trap via coupling capacitors.

The trapped $[Ar\text{-}N_2]^+$ ions are irradiated with femtosecond intense laser pulses (λ = 800 nm, Δt = 40 fs, I = 1.9–3.1×10^{14} W/cm^2) to induce the photodissociation, and immediately after the laser pulse irradiation, the fragment ions, Ar^+ and N_2^+, and the remaining $[Ar\text{-}N_2]^+$ ions are extracted by the pulsed voltage applied to the end-cap electrodes of the ion trap for TOF mass spectrometry.

The timing chart of the experiment is shown in Fig. 2.2(b). The pulsed skimmed molecular beam of the sample gas is introduced into the ion trap four times at an interval of 5 ms. During the first half of the gas injection period, ~50 shots of the ionization laser pulses are focused onto the center of the ion trap to generate Ar^+ and N_2^+ and these ion species are stored in the ion trap. Next, the ionization laser pulses are blocked by a mechanical beam shutter. During the latter half of the gas injection period, the stored Ar^+ and N_2^+ collide with neutral Ar and N_2, and $[Ar\text{-}N_2]^+$ ions in the electronic ground state are generated through the collisional processes. Subsequently, during the waiting period of 3.83 s, neutral Ar and N_2 leave from the ion trap by diffusion while the trapped ions are kept stored. Then, all the stored ions except for $[Ar\text{-}N_2]^+$ ions are removed from the ion trap by the SWIFT method by the SWIFT-RF voltages applied for the next 0.14 s, so that only the $[Ar\text{-}N_2]^+$ ions are stored in the ion trap. After that, the trap-RF voltage is switched off, and the stored $[Ar\text{-}N_2]^+$ ions are irradiated with a fragmentation laser pulse (λ = 800 nm, Δt = 40 fs, I = 1.9–3.1×10^{14} W/cm^2) after the mechanical shutter is completely opened.

Because the response time (13 ms) of the mechanical shutter is longer than the pulse-to-pulse separation (200 μs) of the 5 kHz laser output, the laser beam profile can be partially clipped during the opening period of the shutter. Therefore, until the mechanical shutter is completely opened, triggers for a Pockels cell of the regenerative amplifier of the laser system are halted so that no laser pulses are generated.

The laser pulse duration is measured by SPIDER® APE GmbH, and is varied in the range between 40 and 400 fs by positive chirping of the laser pulses. The polarization direction of the laser pulses is set to be parallel to the TOF axis, and the laser pulses are focused onto the central area of the ion trap with an f = 500 mm plano-convex lens. The laser beam profile at the focal spot is measured by a beam profiler. It is confirmed that the laser beam has a clean Gaussian profile and that the beam waist diameter is 140 μm. There is an inevitable timing jitter of ±1 μs for the switch-off time of the trap-RF voltage, called hereafter the RF-off time. In order that the positive delay of the fragmentation-laser irradiation with respect to the RF-off time is secured, the time delay of the fragmentation laser pulse with respect to the mean RF-off time is set to be 1.2 μs.

The generated fragment ions, Ar^+ and N_2^+, and the remaining $[Ar\text{-}N_2]^+$ ions are extracted from the ion trap by pulsed high-voltages applied to the respective end-cap electrodes of the ion trap, and these ions are recorded by TOF mass spectrometry. Because the signals of the fragment ions are extremely weak, the ion counting scheme is adopted to increase the signal-to-noise ratio of the mass spectra, that is, the discrimination of the ion signals appearing in each shot of the TOF mass data is performed after the single-shot mass spectral data are transferred to a personal computer. After the accumulation of the TOF mass data, the next sequence of the measurement is started by the injection of the sample gas into the ion trap. This sequence is repeated at the repetition rate of 0.25 Hz, that is, at the interval of 4 s.

Because the number density of $[Ar\text{-}N_2]^+$ ions is extremely low (~10^4 cm^{-3}), which is estimated by the calibration of the peak intensity of $[Ar\text{-}N_2]^+$ in the mass spectrum, the number densities of residual gases of neutral Ar and N_2 in the ion trap at the timing of the fragmentation-laser irradiation need to be lowered as much as possible so that Ar^+ and N_2^+ generated from the photodecomposition of $[Ar\text{-}N_2]^+$ can securely be identified in the TOF mass spectrum even though those generated from the photoionization of residual gasses of neutral Ar and N_2 coexist. The

electrodes of the ion trap are cooled down by liquid nitrogen so that the number of the residual gases in the ion trap is reduced. By this cryogenic cooling, the background pressure of the vacuum chamber recorded by a vacuum gauge is kept at around 5×10^{-8} Pa, corresponding to the gas number density of 5×10^{7} cm^{-3}, during the measurements. Because the background pressure inside the ion trap is expected to be much lower than 5×10^{-8} Pa, the estimated gas number density of 5×10^{7} cm^{-3} can be recognized as the upper limit.

When the ion signals from the background gases are recorded, all the stored ions including $[Ar\text{-}N_2]^+$ are ejected from the ion trap by the SWIFT method before the irradiation of the fragmentation laser pulse. When all the stored ions are ejected from the trap, typical signal counts of Ar^+ and N_2^+ ions are 40 and 290 per accumulation cycle, respectively, while those accumulated when $[Ar\text{-}N_2]^+$ ions are trapped are 1600 and 2900 per accumulation cycle.

The cryogenic cooling facilitates also the formation of $[Ar\text{-}N_2]^+$ through the collisions between stored Ar^+ and N_2^+ and neutral Ar and N_2 gases in the ion trap. If we adopt the dissociation energy of $[Ar\text{-}N_2]^+$ of D_0 = 1.06 eV determined by Teng and Conway using the thermochemical method,[5] which corresponds to 1.23×10^4 K, the collision induced dissociation of $[Ar\text{-}N_2]^+$ at 77 K can be neglected. It has been known that the vibrational temperature of trapped molecular ions becomes close to the buffer gas temperature when storing time is of the order of 100 ms.[46] Because the storing time in the present experiment, 3.97 s (= 3.83 s + 0.14 s), is sufficiently long, the vibrational temperature of the trapped $[Ar\text{-}N_2]^+$ ions just before the irradiation of the fragmentation laser pulse is considered to be close to the liquid nitrogen temperature. Using the vibrational frequencies of the normal modes of $[Ar\text{-}N_2]^+$;[9] ν_1 (N-N stretching) = 2344 cm^{-1}, ν_2 (Ar-N_2 stretching) = 311 cm^{-1}, and ν_3 (Ar-N_2 bending) = 179 cm^{-1}, the populations in the vibrationally excited states of the ν_1, ν_2, and ν_3 modes are estimated to be 9×10^{-20}, 3×10^{-3}, and 4×10^{-4} at 77 K. Therefore, 99.7% of the stored dimer ions, $[Ar\text{-}N_2]^+$, are considered to be in the vibrational ground state.

2.3. Results and discussion

2.3.1. Ion-trap mass spectroscopy

In order to investigate the photodecomposition processes of $[Ar\text{-}N_2]^+$ ions, $[Ar\text{-}N_2]^+$ ions need to be stored exclusively before the irradiation of a near-IR femtosecond laser pulses to induce their photodissociation. As shown in Fig. 2.3, a mass spectrum of the trapped ions recorded after the mass-selective accumulation of $[Ar\text{-}N_2]^+$ exhibits only a single peak at m/z = 68, which confirms that the mass-selective accumulation of $[Ar\text{-}N_2]^+$ was achieved in the ion trap.

Figure 2.4 is a mass spectrum of the ions generated when the stored $[Ar\text{-}N_2]^+$ ions were irradiated with a near-IR femtosecond laser pulses at the laser field intensity of 3.1×10^{14} W/cm^2. The ion signals of N_2^+ (m/z = 28) and Ar^+ (m/z = 40) appearing in Fig. 2.4 show that both Eqs. (2.5) and (2.6) proceed by the absorption of the near-IR laser pulses. Because the present voltage conditions for the electrodes are not in the time-lag energy focusing conditions,[47] the initial momenta of fragment

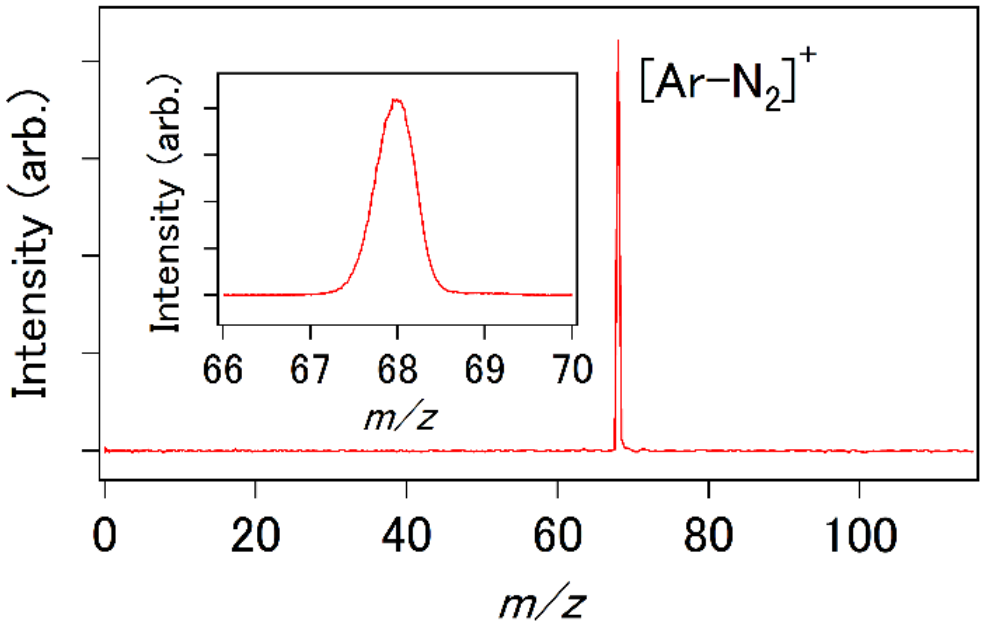

Figure 2.3. The mass spectrum of the trapped ions after the mass-selective ion accumulation of $[Ar\text{-}N_2]^+$ ions. The inset shows an expanded view at around m/z = 68, showing that $[Ar\text{-}N_2]^+$ is exclusively trapped in the ion trap.

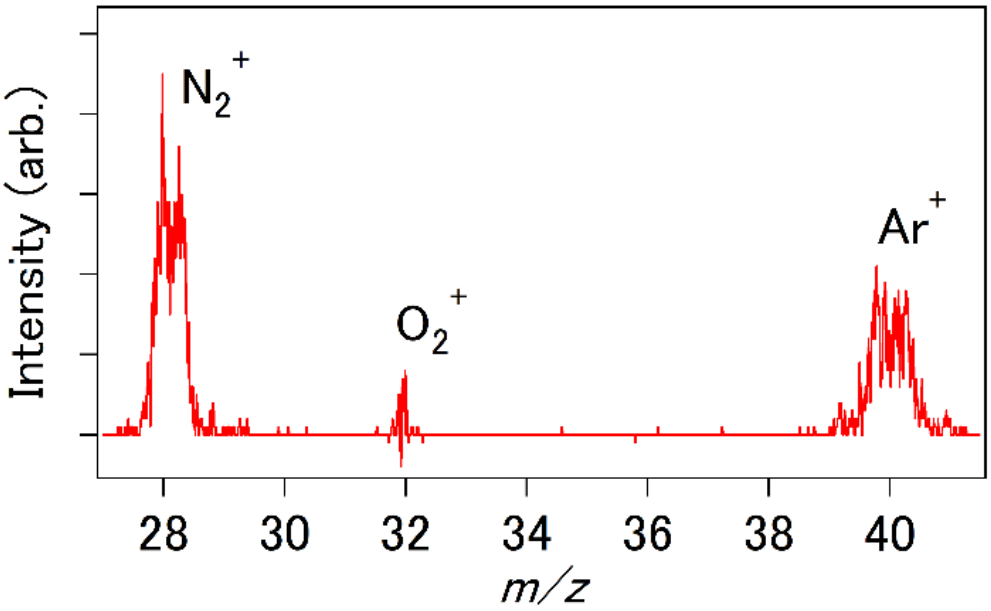

Figure 2.4. The mass spectrum of the fragment ions generated by the photodecomposition of the trapped $[Ar\text{-}N_2]^+$ induced by the irradiation of a femtosecond laser pulse (λ = 800 nm, Δt = 40 fs, $I = 3.1\times10^{14}$ W/cm^2). The small peak of O_2^+ (m/z = 32) identified in the mass spectrum originates from the photoionization of O_2 in the background residual gas.

ions are reflected to their TOF. Therefore, the broad double-peak profiles of N_2^+ and Ar^+ in Fig. 2.4 indicate that these fragment ions have recoil momenta to the forward and backward directions along the TOF axis.

By comparing the observed peak profiles of the fragment ions, N_2^+ and Ar^+, with those obtained by ion trajectory simulations, the released kinetic energies for both of the two fragmentation channels (5) and (6) are determined to be 0.25(5) eV and 0.32(7) eV, respectively. These values of the released kinetic energies are consistent with the kinetic energies of 0.22 and 0.31 eV (See Fig. 2.1) that can be released when the photoexcited $[Ar\text{-}N_2]^+$ at 800 nm is decomposed into Ar (^{1}S) + N_2^+ (X $^2\Sigma_g^+$) (v_{ion} = 1) and Ar^+ ($^2P_{3/2}$) + N_2 (X $^1\Sigma^+_g$)) (v = 0).

In the numerical simulations of the trajectories of the ions performed using SIMION 8.0.4,[48] the trajectories are started from the central point in the ion trap and terminated at the end of the TOF tube where the ion detector is located. In the simulation, it is assumed that the initial positions of ions are homogenously distributed in the cylindrical-shaped spatial area whose length and diameter are 1.0 mm and 0.14 mm, respectively. The length corresponds to the diameter of the disk-shape area in which ions are trapped in the central point of the ion trap, and the diameter of 0.14 mm corresponds to the focal diameter of the laser pulses. The initial kinetic energy of the complex ions, $[Ar\text{-}N_2]^+$, is assumed to be 0.10 eV and the isotropic distribution is assumed for the direction of the initial velocity vector of the ions. It is also assumed that the complex ions, $[Ar\text{-}N_2]^+$, are randomly oriented in space and are photodissociated by the irradiation of the laser pulse whose polarization direction is parallel to the TOF axis, that is, both the angular distribution of the ejection direction of N_2^+ through Eq. (2.3) and that of Ar^+ through Eq. (2.4) are represented by $\cos^2\theta$, where θ is the polar angle measured from the TOF axis. A total of 50,000 trajectories are run in the numerical simulation for both channels of Eq. (2.5) and Eq. (2.6).

2.3.2. Photodissociation pathways

As shown in Fig. 2.1, the dissociation limits of the photodissociation channels, (5) and (6), measured from the vibrational ground state of the electronic ground state of $[Ar\text{-}N_2]^+$ are 1.33 eV and 1.24 eV, respectively. Because the photon energy of an 800 nm laser pulse is 1.55 eV, the following four dissociation limits are energetically allowed after the one-photon excitation (See Appendix A for the confirmation that the excitation is achieved by one photon absorption.): (i) $Ar(^1S) + N_2^+(X\ ^2\Sigma_g^+)$ ($v_{ion} = 0$), (ii) $Ar(^1S) + N_2^+(X\ ^2\Sigma_g^+)$ ($v_{ion} = 1$), (iii) $Ar^+(^2P_{3/2}) + N_2(X\ ^1\Sigma_g^+)$ ($v = 0$), and (iv) $Ar^+(^2P_{1/2}) + N_2(X\ ^1\Sigma_g^+)$ ($v = 0$). Note that the potential energy curve of $Ar^+(^2P_{1/2})\cdots N_2(X\ ^1\Sigma_g^+)$ ($v = 0$) correlated to the dissociation limit of $Ar^+(^2P_{1/2}) + N_2(X\ ^1\Sigma_g^+)$ ($v = 0$) cannot be accessed from the electronic ground $Ar(^1S)\cdots N_2^+(X\ ^2\Sigma_g^+)$ by the absorption of an 800 nm photon because of a lack of the Franck-Condon

overlap. Indeed, as can be seen in Fig. 2.1, the Franck-Condon region represented by the hatched box area does not have an overlap with the repulsive part of the potential energy curves of $Ar^+(^2P_{1/2})\cdots N_2(X^1\Sigma_g^+)$ (v = 0, 1, 2, ...). Therefore, the dissociation will not lead to $Ar^+(^2P_{1/2})$ + $N_2(X\ ^1\Sigma_g^+)$ (v = 0), and the photodissociation can proceed only through the following three channels;

$$[Ar\text{-}N_2]^+ + h\nu \rightarrow Ar(^1S) + N_2^+(X\ ^2\Sigma_g^+)\ (v_{ion} = 0). \quad (2.8)$$

$$[Ar\text{-}N_2]^+ + h\nu \rightarrow Ar(^1S) + N_2^+(X\ ^2\Sigma_g^+)\ (v_{ion} = 1). \quad (2.9)$$

$$[Ar\text{-}N_2]^+ + h\nu \rightarrow Ar^+(^2P_{3/2}) + N_2(X\ ^1\Sigma_g^+)\ (v = 0). \quad (2.10)$$

The excess energies of the dissociation channels, Eqs. (2.8), (2.9), and (2.10), after the one-photon excitation at 800 nm are 0.49, 022, and 0.31 eV, respectively. As explained above in Section III.A, the

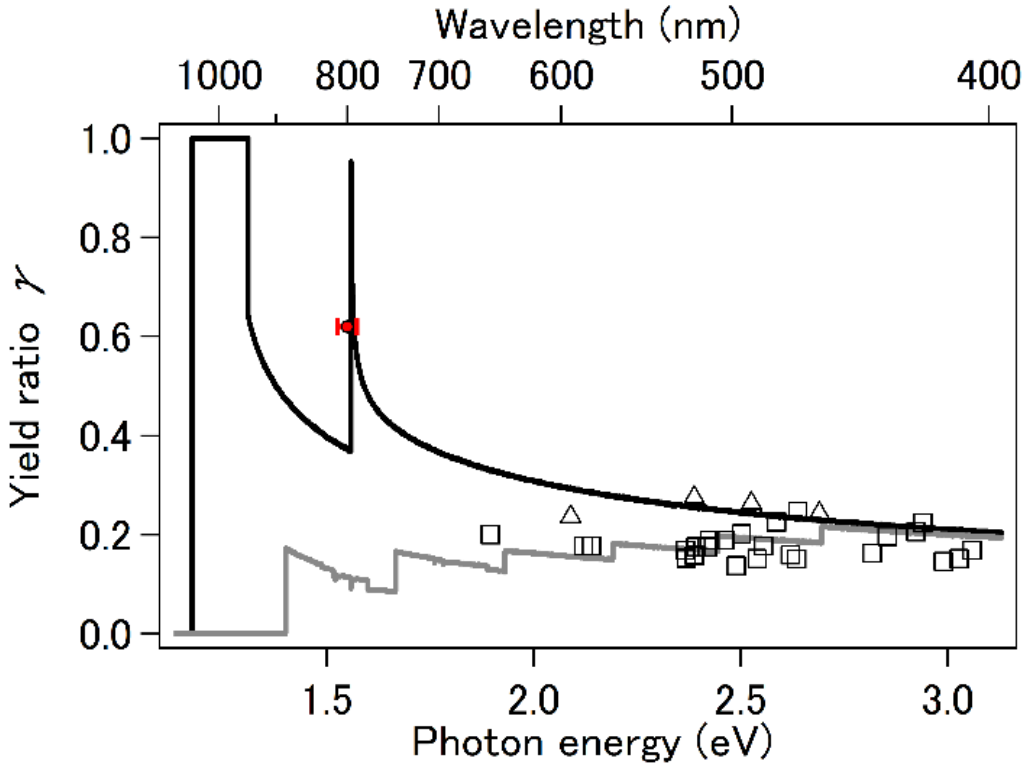

Figure 2.5. The yield ratio of N_2^+ produced from $[Ar\text{-}N_2]^+$ as a function of the excitation photon energy calculated by the Landau-Zener-Stückelberg model (gray line) and the IVR model (black line). The yield ratios obtained experimentally in the present study (red short horizontal bar), Ref. 40 (triangles) and Ref. 41 (squares) are also plotted.

released kinetic energies, 0.25(5) eV and 0.32(7), determined from the broadening of the peaks in the mass spectrum, show that the dissociation proceeds mainly thorough Eqs. (2.9) and (2.10), which means that Eq. (2.8) has a minor contribution.

As shown in Fig. 2.5, the yield ratio, γ, given by Eq. (2.7) for the intra-complex charge transfer reaction, Eq. (2.5), producing N_2^+ ($X\ ^2\Sigma_g^+$) ($v_{ion} = 1$) and N_2^+ ($X\ ^2\Sigma_g^+$) ($v = 0$), is determined to be $\gamma = 0.62$ (red circle), which is more than three times as large as the ratios obtained by the irradiation of UV and visible nanosecond laser pulses ($\gamma \sim 0.2$) reported in the previous studies.[40,41] This large value of γ obtained in the present study indicates that the intra-complex charge transfer reaction of $[Ar\text{-}N_2]^+$ is significantly enhanced by the irradiation of the near IR (800 nm) ultrashort laser pulses.

The enhancement of the yield ratio γ at 800 nm shows that the adiabatic population transfer of the electronically excited complexes of $Ar^+(^2P_{3/2})\cdots N_2$ to $Ar\cdots N_2^+$ proceeds more efficiently at 800 nm than at the shorter wavelength. Because the slower nuclear motion can enhance the probabilities of adiabatic population transfer in molecular dissociation,[44–46] the enhancement of γ at 800 nm is consistent with the fact that the excess energy above the dissociation limits at the photoexcitation at 800 nm is lower than that at the shorter wavelength adopted in the previous studies.[40,41]

2.3.3. Adiabatic and non-adiabatic population transfer

It can be seen in Fig. 2.1 that the potential energy curves of $Ar^+(^2P_{3/2})\cdots N_2$ ($X\ ^1\Sigma_g^+$) ($v = 0$, 1, ...) cross the potential energy curves of $Ar\cdots N_2^+(X\ ^2\Sigma_g^+)$ ($v_{ion} = 1, 2, \ldots$). Because of the charge exchange interaction, these crossings become avoided crossings, exhibiting the energy gap separating a pair of the adiabatic potential curves. Hereafter, the avoided crossing between the potential energy curve of $Ar^+(^2P_{3/2})\cdots N_2(X^1\Sigma_g^+)$ (v) and that of $Ar\cdots N_2^+(X^2\Sigma_g^+)$ (v_{ion}) will be denoted as the (v, v_{ion}) crossing.

When the vibrational wave packet reaches the avoided crossings, the charge transfer reaction can proceed on the adiabatic potential as long as the nuclear motion at the avoided crossing is sufficiently slow. On the other hand, when the nuclear motion at the crossings becomes faster, the non-adiabatic transition proceeds more efficiently at the avoided crossings, resulting in the suppression of the charge transfer.

According to the Landau-Zener-Stückelberg (LZS) model,[49–51] the probability of the non-adiabatic transition at the (v, v_{ion}) crossing can be represented as

$$P(v_{\mathrm{R}}) = \exp\left[-\frac{2\pi H(R, v, v_{\mathrm{ion}})^2}{\hbar v_R \Delta}\right], \tag{2.11}$$

where R is the intermolecular distance at the crossing, Δ is the absolute value of the difference in the slopes of the potential energy curves, $H(R, v, v_{\mathrm{ion}})$ is the matrix element of the vibronic coupling at the crossing, and v_{R} is the magnitude of the relative velocity at the crossing. The relative velocity, v_{R}, is evaluated by

$$v_{\mathrm{R}} = \left[\frac{2}{\mu}\left(h\nu - E_0\right)\right]^{\frac{1}{2}} = \left[\frac{2}{\mu}\Delta E\right]^{\frac{1}{2}}, \tag{2.12}$$

where $h\nu$ is the photon energy, E_0 is the potential energy at the crossing, and ΔE defined as $h\nu - E_0$ represents the excess energy at the crossing.

For the high-energy collisional charge transfer reactions of $Xe(^3P_{0,2}) + N_2(X)$[52], $Na + N_2$,[53] $Na + CO$,[53] $I_2 + M$ (M = Li, Na, K, Rb, Cs, and Tl)[54] where the time scale of the non-adiabatic transition, $\tau_{\text{non-ad}}$, is much shorter than the vibrational periods of the N_2 and N_2^+ moieties, $\tau_{\mathrm{vib}} \sim 14$ fs and 15 fs, respectively, $H(R, v, v_{\mathrm{ion}})$ can be factorized into two factors as

$$H(R, v, v_{\mathrm{ion}})^2 = H(R)^2 q(v, v_{\mathrm{ion}}), \tag{2.13}$$

where $H(R)$ is the matrix element of the vibronic coupling between the two electronic states and $q(v, v_{\mathrm{ion}})$ is the Franck-Condon factor for the $v \leftarrow v_{\mathrm{ion}}$ transition.[42] On the other hand, when $\tau_{\text{non-ad}}$ is

sufficiently long so that it becomes comparable with or longer than τ_{vib},[34,55] $H(R, v, v_{ion})$ becomes independent of the vibrational quantum numbers and can be expressed as

$$H(R, v, v_{ion}) = H(R), \tag{2.14}$$

and consequently, the probabilities of the non-adiabatic transition at the avoided crossings for all the (v, v_{ion}) crossings can be expressed as

$$P(v_R) = \exp\left[-\frac{2\pi H(R)^2}{\hbar v_R \Delta}\right]. \tag{2.15}$$

Using the numerical values of R, E_0, Δ, and $H(R)$ for the 20 lowest-lying avoided crossings, which were tabulated in Table 1 in Ref. 39, the $\tau_{non\text{-}ad}$ values are evaluated using the formula,[12,56]

$$\tau_{non\text{-}ad} = \left[\left(\frac{\hbar}{2v_R\Delta}\right)^2 + \left(\frac{H(R)}{v_R\Delta}\right)^4\right]^{1/4}. \tag{2.16}$$

20 lowest-lying avoided crossings are shown as the filled circles in Fig. 2.1.

For example, when the photon energy is 2.1 eV, corresponding to the wavelength of 590 nm, the $\tau_{non\text{-}ad}$ values calculated for the 20 avoided crossings located below the excitation energy are distributed around the mean value of 4.1 fs with the standard deviation of 1.0 fs. Because the $\tau_{non\text{-}ad}$ values are the same order of magnitude as τ_{vib}, it can be assumed that the matrix elements of the vibronic coupling are independent of v and v_{ion} as expressed in Eq. (2.14). Therefore, in the numerical simulation of the bifurcations at the respective crossing points described below, Eq. (2.15) is adopted as the non-adiabatic transition probability.

2.3.4. Numerical simulations of adiabatic and non-adiabatic population transfer

In the numerical simulations of the intra-complex charge transfer processes using Eq. (2.15), the initial photon energy is varied in the range between 1.13 eV (1,097 nm) and 3.13 eV (396 nm) at intervals of 0.4 meV. It is assumed that the complex is photoexcited to the potential curve correlated

to the dissociation limit of $Ar^+(^2P_{3/2})$ + N_2 ($X^1\Sigma_g^+$) (v = 0) and the bifurcation calculation is started from the inner wall of the potential energy curve at the energy accessed by the given photon energy.

For example, at the excitation energy of 1.55 eV (800 nm), as shown in Fig. 2.6, which is an expanded view of the related part of the potential energy curves and their crossings shown in Fig. 2.1, the bifurcation calculation is started from the point marked with "Start". Because of the negative slope of the start point, the complex moves towards the leftmost crossing point, C1, and the bifurcation occurs according to the probability calculated by Eq. (2.15). The complex that chooses the adiabatic

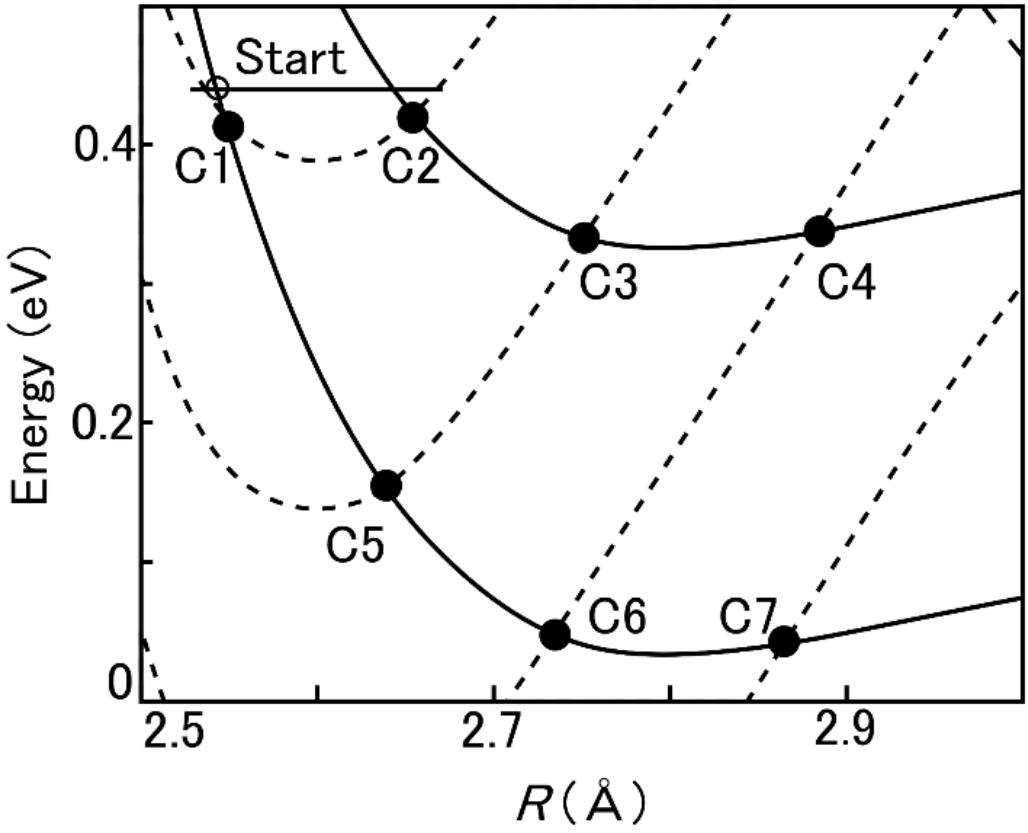

Figure 2.6. The enlarged part in the intra-complex potentials shown in Fig. 2.1. The horizontal bar represents the excitation energy given by a femtosecond laser pulse (λ = 800 nm, Δt = 40 fs). The bifurcation simulation starts from the point specified by the open circle. The bifurcation processes occur in the enlarged domain at the avoided crossing denoted as C1, C2, …., C7.

pathway at C1 moves towards the crossing point C2, and the bifurcation occurs at C2 according to the probability calculated by Eq. (2.15). This pathway can be written as

Start → C1(forward, adiabatic) → C2(forward, adiabatic) → C3 …..

In a similar manner, we can also find the pathway,

Start → C1(forward, nonadiabatic) → C5(forward, adiabatic) → C3 ….

It is also possible that the complex can move towards the backward direction. For example, we can find the following oscillation pathway,

Start → C1(forward, adiabatic) → C2(forward, nonadiabatic) →

C2(backward, nonadiabatic) → C1(backward, adiabatic) →

C1 (forward, adiabatic) → C2….

At each of the crossing point, the bifurcation is judged by a random number generated in the range between 1 and 0, so that the non-adiabatic or adiabatic pathway is chosen by the numerical value of the random number based on the nonadiabatic transition probability calculated by Eq. (2.15). We perform this bifurcation calculation until the complex dissociates. For a given photon energy, I perform the bifurcation calculations 30,000 times. Because I vary the initial photon energy with intervals of 0.4 meV in the range of 1.13–3.13 eV eV, I perform the bifurcation calculations a total of 1.5×10^8 times.

The gray line in Fig. 2.5 shows the results of the bifurcation calculations of the yield ratio γ as a function of the excitation photon energy. We perform the bifurcation calculations until the complex dissociates. The threshold appearing at 1.40 eV corresponds to the energy threshold for the opening of the dissociation channel, $Ar(^1S) + N_2^+(X\ ^2\Sigma_g^+)$ (v_{ion} = 1). The gradual decrease in the yield ratio γ above the threshold as a function of the photon energy can be ascribed to the increase in the relative velocity v_R given by Eq. (2.12) at the avoided crossings, leading to the increase in the yield of the non-adiabatic pathway to produce $Ar^+(^2P_{3/2}) + N_2\ (X^1\Sigma_g^+)$. When the photon energy increases

further and exceeds the second threshold above which the next higher-lying channel yielding Ar(^{1}S) + N_2^+($X\ ^2\Sigma_g^+$) (v_{ion} = 2) becomes open, the yield ratio γ increases stepwise associated with the opening of the new channel, followed by a gradual decrease by the same reason described above for the lowest-energy channel. As the photon energy increases further, a similar stepwise increase and gradual decrease in γ occurs repeatedly as shown in Fig. 2.5 as the new dissociation channels producing N_2^+($X^2\Sigma_g^+$) with the larger vibrational quantum numbers of v_{ion} = 3, 4, 5, and 6 open successively.

In the larger photon energy region above 1.91 eV, γ takes the value between 1.9 and 2.7, which are in good agreement with the experimental results (γ=0.21–0.28) reported by Kim et al.[40] in the range of 357–590 nm and those (γ = 0.13–0.25) reported by Magnera et al.[41] in the range of 270–650 nm. On the other hand, the yield ratio at 1.55 eV (corresponding to 800 nm) is calculated to be 0.11, which is much smaller than 0.62 obtained experimentally in the present study. This means that the bifurcation simulation above underestimates the probability of the adiabatic population at the crossings between the potential energy curves leading to the production of N_2^+ ($X^2\Sigma_g^+$).

2.3.5. Numerical simulations with intra-complex energy transfer

In the bifurcation simulations above, at the photon energy of 1.55 eV, N_2^+($X\ ^2\Sigma_g^+$) can be created only when the bifurcation along the forward direction at the crossing between "Ar^+ ($^2P_{3/2}$)···N_2 ($X^1\Sigma_g^+$) (v = 0)" and "Ar (^{1}S)···N_2^+ ($X^2\Sigma_g^+$) (v_{ion} = 1)" chooses the adiabatic pathway, leading to the dissociation into Ar (^{1}S) + N_2^+ ($X^2\Sigma_g^+$) (v_{ion} = 1). However, it is possible that the intra-complex vibrational energy transfer from the vibrationally excited N_2^+($X\ ^2\Sigma_g^+$) moiety in the complex, Ar(^{1}S)···N_2^+($X\ ^2\Sigma_g^+$) ($v_{ion} \geq 1$), to the intra-complex stretching vibrational mode induces the dissociation of the complex into Ar(^{1}S) + N_2^+($X^2\Sigma_g^+$) (v_{ion} = 0 and 1), leading to the increase in the yield ratio of N_2^+($X\ ^2\Sigma_g^+$).

Therefore, as a next step, this intra-complex vibrational energy redistribution (IVR) via the anharmonic coupling among the vibrational modes of the complex is included in the bifurcation calculations based on the LZS model adopted above. In this model, once a trajectory takes the adiabatic pathway at an avoided crossing to form $Ar(^1S)\cdots N_2^+(X^2\Sigma_g^+)$ (v_{ion}) with $v_{ion} \geq 1$, the trajectory is regarded as that leads eventually to the dissociation into $Ar(^1S) + N_2^+(X^2\Sigma_g^+)$ ($v_{ion} = 0$ or 1). Therefore, in this model, as long as the IVR process turns on at the avoided crossing, the decomposition proceeds regardless of the rate of the IVR. For example, at the excitation energy of 1.55 eV (800 nm), if the complex chooses the adiabatic pathway at the first crossing point, C1, the complex is prepared in $Ar(^1S)\cdots N_2^+(X\ ^2\Sigma_g^+)$ ($v_{ion} = 6$) via the charge transfer, which automatically leads to the dissociation into $Ar(^1S) + N_2^+(X^2\Sigma_g^+)$ ($v_{ion} = 0$ or 1) by the IVR. Of course, the complex can take the non-adiabatic pathway at the C1 crossing, but the complex can lead to the IVR-induced dissociation when it chooses the adiabatic pathway at the next crossing point, C5. The γ values obtained by the numerical simulation in which the IVR assisted dissociation is included are shown with the black line in Fig. 2.5. We run the bifurcation calculations in the same manner as in the cases in which the IVR is not taken into account.

It should be noted that, in the case of this IVR model, the yield ratio can be calculated more straightforwardly as the sum of the products of the probability of arriving at a crossing point and the probability of the adiabatic population transfer along the potential energy curve of $Ar^+(^2P_{3/2})\cdots N_2(X\ ^1\Sigma^+_g)$ ($v = 0$). We confirm that the yield ratio represented as a function of the excitation photon energy obtained by this straightforward method reproduces in a perfect manner the black line in Fig. 2.5 obtained after performing the bifurcation calculations 30,000 times.

The black line exhibits the first threshold at 1.175 eV, corresponding to the energy of the avoided crossing between the potential curve of the initially prepared $Ar^+(^2P_{3/2})\cdots N_2(X\ ^1\Sigma_g^+)$ ($v = 0$) and that of $Ar(^1S)\cdots N_2^+(X\ ^2\Sigma_g^+)$ ($v_{ion} = 3$). Above the first threshold, the yield ratio γ keeps taking the

value of $\gamma = 1$ until the photon energy reaches 1.310 eV, corresponding to the dissociation limit of $Ar^+(^2P_{3/2}) + N_2(X\ ^1\Sigma_g^+)$ ($v = 0$). As the photon energy increases further, the yield ratio γ gradually decreases, reflecting the fact that the relative velocity v_R at the avoided crossings becomes larger.

When the photon energy reaches $h\nu = 1.55$ eV, corresponding to the wavelength (800 nm) of the laser pulses employed in the present experiment, γ increases largely to exhibit a spike-like feature whose peak height becomes as large as ~1.0. This enhancement of γ can be ascribed to the efficient adiabatic population transfer at the avoided crossing between the potential curve of the initially prepared $Ar^+(^2P_{3/2})\cdots N_2(X^1\Sigma_g^+)$ ($v = 0$) and that of $Ar(^1S)\cdots N_2^+(X\ ^2\Sigma_g^+)$ ($v_{ion} = 6$).

At the laser wavelength of 800 nm, the relative velocity at this avoided crossing should be very small, the probability of the complex to take the non-adiabatic pathway becomes extremely small according to Eq. (2.15), that is, the probability of the complex to take the adiabatic pathway become closed to 1. Because the IVR process follows the adiabatic population transfer in the IVR-induced dissociation model, the complex is decomposed into $Ar(^1S) + N_2^+(X\ ^2\Sigma_g^+)$ ($v_{ion} = 0$ and 1) after the avoided crossing located at 1.558 eV.

As shown in Fig. 2.5, the γ value, $\gamma = 0.62$, obtained in the present study at the photon energy of 1.55 eV plotted with a filled circle red circle in Fig. 2.5, is consistent with the results of the numerical simulations considering that the spectral bandwidth of the femtosecond (40 fs) laser pulse covers the energy range of 1.53–1.57 eV, corresponding to the wavelength range of 812–788 nm. When the photon energy increases further, the yield ratio gradually decreases because the velocity at the avoided crossings increases and the probability of the non-adiabatic transition increases at the avoided crossings, resulting in the decrease in γ, which is also in good agreement with the previous experimental results recorded at the higher photon energies. Therefore, it is highly probable that the dissociation of the photoexcited $[Ar\text{-}N_2]^+$ complexes proceeds via the adiabatic population transfer at the avoided crossings accompanied by the intra-complex charge transfer followed by the IVR, through

which the vibrational energy of the N_2^+ moiety is transferred to the intra-complex stretching vibrational mode, leading to the dissociation.

A similar enhancement of γ is expected at the avoided crossings between the potential curve of the initially prepared $Ar^+(^2P_{3/2})\cdots N_2(X^1\Sigma_g^+)$ (v = 0) and that of $Ar(^1S)\cdots N_2^+(X\ ^2\Sigma_g^+)$ (v_{ion} > 6). For v_{ion} = 7 and 8, the enhancement can appear at around 527 and 396 nm, respectively. However, as shown in Fig. 2.5, such enhancement was not identified in the previous measurements[40, 41] performed using ns laser pulses in the shorter wavelength region. It is possible that the resonance enhancement occurs only in the close vicinity of the resonance energies of these crossing points located in the shorter excitation wavelength region.

2.4. Conclusion

By the ion-trap mass spectrometry, the photodissociation processes of $[Ar\text{-}N_2]^+$ ions induced by the irradiation of a 800 nm femtosecond intense laser pulse have been investigated. The yield ratio γ of N_2^+ with respect to the sum of the yields of Ar^+ and N_2^+ has been determined to be γ = 0.62, which is significantly larger than $\gamma \sim$ 0.2 reported before when the photodissociation is induced by UV and visible light.[40,41] From the numerical simulations based on the model in which the dissociation to form N_2^+ proceeds via an intra-complex vibrational energy transfer after the adiabatic population transfer accompanied by the intra-complex charge transfer at the avoided crossings between the potential energy curve of $Ar^+(^2P_{3/2})\cdots N_2(X^1\Sigma_g^+)$ (v = 0) and the potential energy curves of $Ar(^1S_0)\cdots N_2^+(X^2\Sigma_g^+)$ (v_{ion} = 1, 2, ...), the variation of γ as a function of the excitation photon energy has been consistently interpreted and the enhancement of γ at 800 nm has been ascribed to the efficient near-resonant adiabatic population transfer from $Ar^+(^2P_{3/2})\cdots N_2(X^1\Sigma_g^+)$ (v = 0) to $Ar(^1S)\cdots N_2^+(X^2\Sigma_g^+)$ (v_{ion} = 6).

Appendix: Confirmation of one-photon transitions

The laser-field intensity employed in the present study is around four orders of magnitude higher than those in the previous studies,[40,41] and therefore, it is possible that multiphoton absorption occurs so that $[Ar\text{-}N_2]^+$ is excited to the higher-lying electronically excited states and that the yield ratio γ varies in response to the changes in the light field intensity.

In order to clarify the contribution from the multiphoton transition, the laser field dependences of the ion fragments, Ar^+ and N_2^+, are examined. As shown in Fig. 2.7(a), the yields of Ar^+ and N_2^+ normalized by the amount of the stored $[Ar\text{-}N_2]^+$ ions increase almost linearly as a function of the laser field intensity, and consequently, the yield ratio γ takes almost constant value between 0.62 and 0.65 in the laser field intensity range of 1.9–3.1×10^{14} W/cm^2. In addition, as shown in Fig. 2.8, the yield ratio exhibits no specific dependence on the laser pulse duration up to 400 fs and takes the values in the range between 0.62 and 0.75, suggesting that no sequential multiphoton excitation proceeds.

Next, the anisotropy in the yields of the fragment ions with respect to the laser polarization dependence is examined. As shown in Fig. 2.9, the angular dependences of the yields of Ar^+ and N_2^+ as well as the sum the yields plotted as a function of the angle θ between the TOF axis and the laser polarization direction are somewhat flatter than the curve obtained when the anisotropy parameter β = 2.0 and the extent of the anisotropy does not show any influence of multiphoton transitions.

Therefore, it can be concluded that the precursor of the electronically excited $[Ar\text{-}N_2]^+$ yielding "$Ar(^1S) + N_2^+(X^2\Sigma_g^+)$" and "$Ar^+(^2P_{3/2}) + N_2(X^1\Sigma_g^+)$" is the electronically excited complex $Ar^+(^2P_{3/2})\cdots N_2^+(X^2\Sigma_g^+)$ prepared by the one-photon excitation from the complex in the electronic ground state, $[Ar\cdots N_2]^+$, as in the cases of the previous experiments performed with much weaker laser field intensities in the visible and UV wavelength regions. The observation that the dissociation processes are induced only by one-photon excitation even in the intense laser fields (1.9–

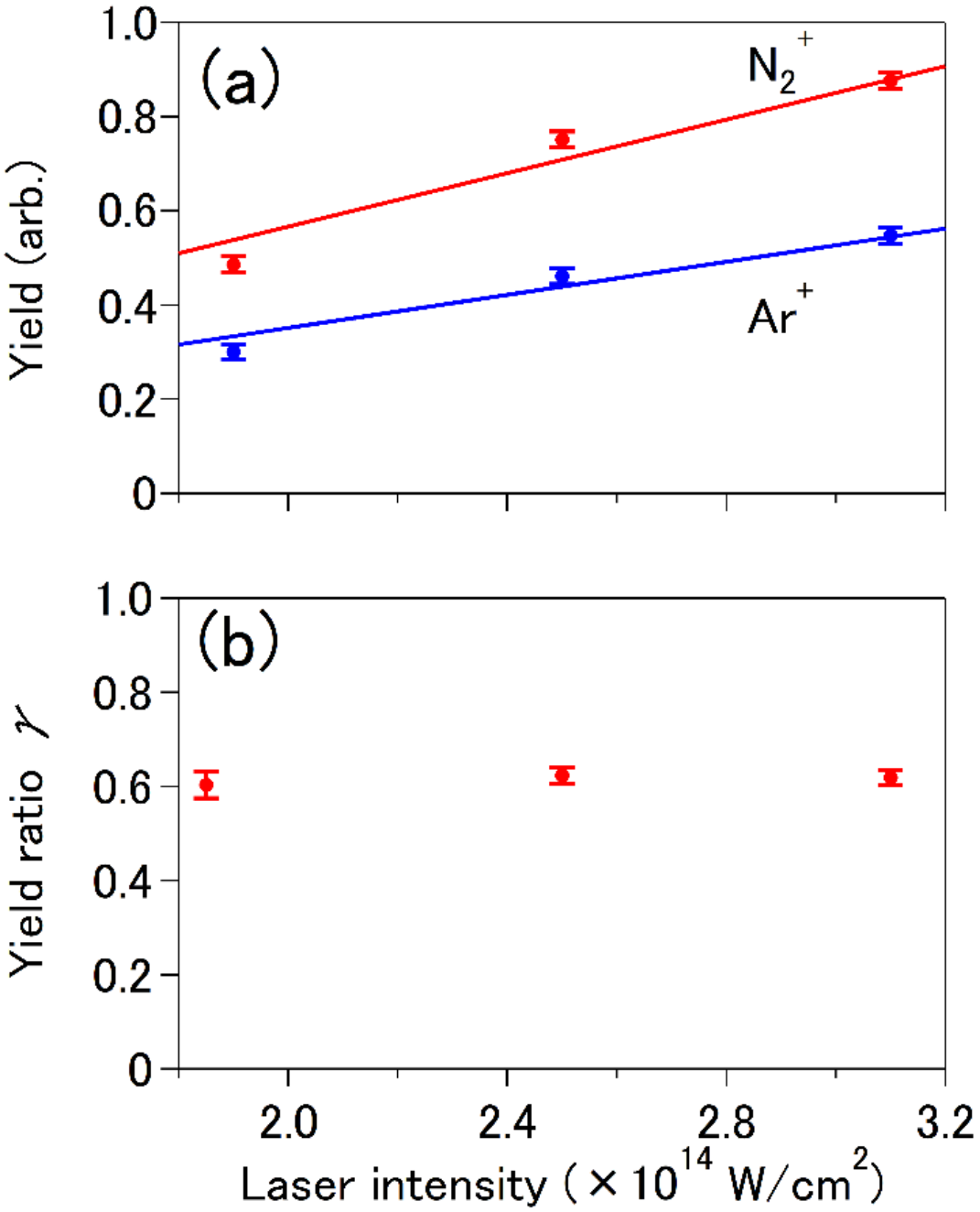

Figure 2.7. (a) The yields of Ar^+ and N_2^+ produced by the irradiation of $[Ar\text{-}N_2]^+$ with a femtosecond laser pulse (λ = 800 nm, Δt = 40 fs) normalized by the yield of $[Ar\text{-}N_2]^+$ and (b) the yield ratio γ of the charge transfer reaction defined by Eq. (2.7) as a function of the laser-field intensity.

3.1×10^{14} W/cm^2) may be ascribed to a small Franck-Condon overlap between the electronic ground $[Ar\text{-}N_2]^+$ state and the first electronically excited state of $Ar^+(^2P_{3/2})\cdots N_2(X\ ^1\Sigma^+_g)$ [Ω = 1/2] at 800 nm.

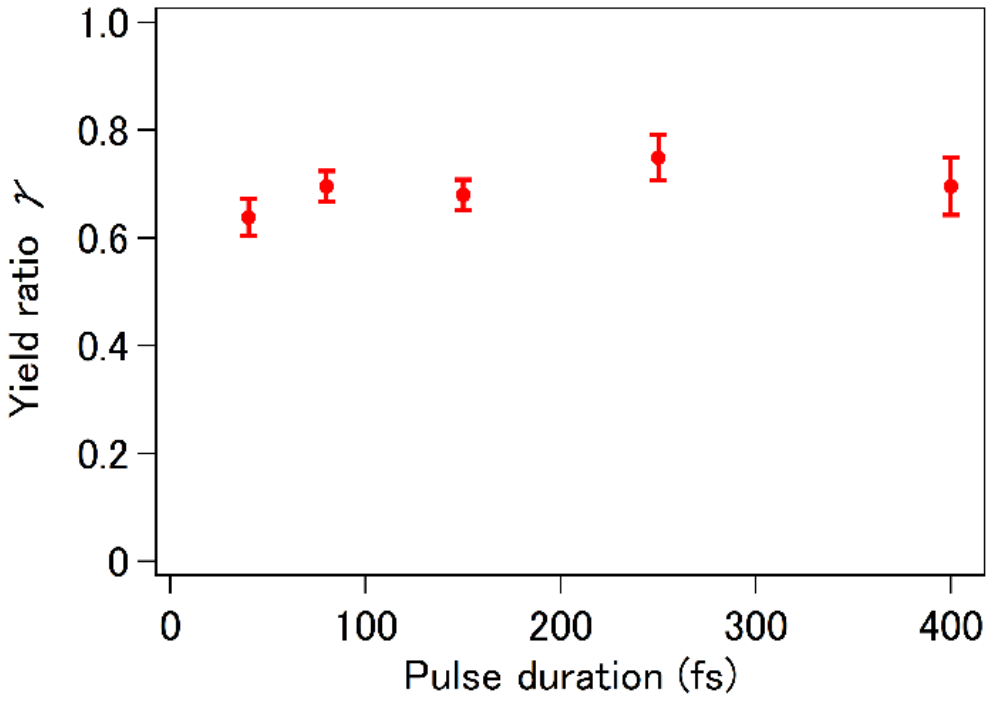

Figure 2.8. The yield ratio γ of N_2^+ produced by the irradiation of $[Ar\text{-}N_2]^+$ with a femtosecond laser pulse (λ = 800 nm) at the five different laser pulse duration: Δt = 40 fs, 80 fs, 150 fs, 250 fs, and 400 fs. Because the distance between the two gratings in the compressor of the femtosecond laser system was varied to make the pulse duration longer, the light field intensity becomes weaker as the pulse duration increases. The laser field intensities were measured to be $I = 3.1\times10^{14}$ W/cm^2, 1.6×10^{14} W/cm^2, 1.0×10^{14} W/cm^2, 6.0×10^{13} W/cm^2, and 3.8×10^{13} W/cm^2 at Δt = 40 fs, 80 fs, 150 fs, 250 fs, and 400 fs, respectively.

As shown in Fig. 2.1, the Franck-Condon overlap is expected to be sufficiently large as long as we adopt the potential energy curves obtained by the semi-empirical multipole expansion. However, it is possible that the potential energy curve of $Ar^+(^2P_{3/2})\cdots N_2(X\ ^1\Sigma^+_g)$ [Ω = 1/2] is slightly more repulsive than that obtained by Candori et al.[12] by the multipole expansion and is closer to that obtained by Langenberg et al.[11] using the preoptimized valence bond method, so that the Franck-Condon overlap at 800 nm becomes much smaller while that in the visible and UV wavelength range is kept to be sufficiently large. Indeed, the wavelength dependence of the photodissociation cross section of $[Ar\text{-}N_2]^+$ [40,41,57] suggests that the electronic transition from $[Ar\text{-}N_2]^+$ in the electronic ground state to

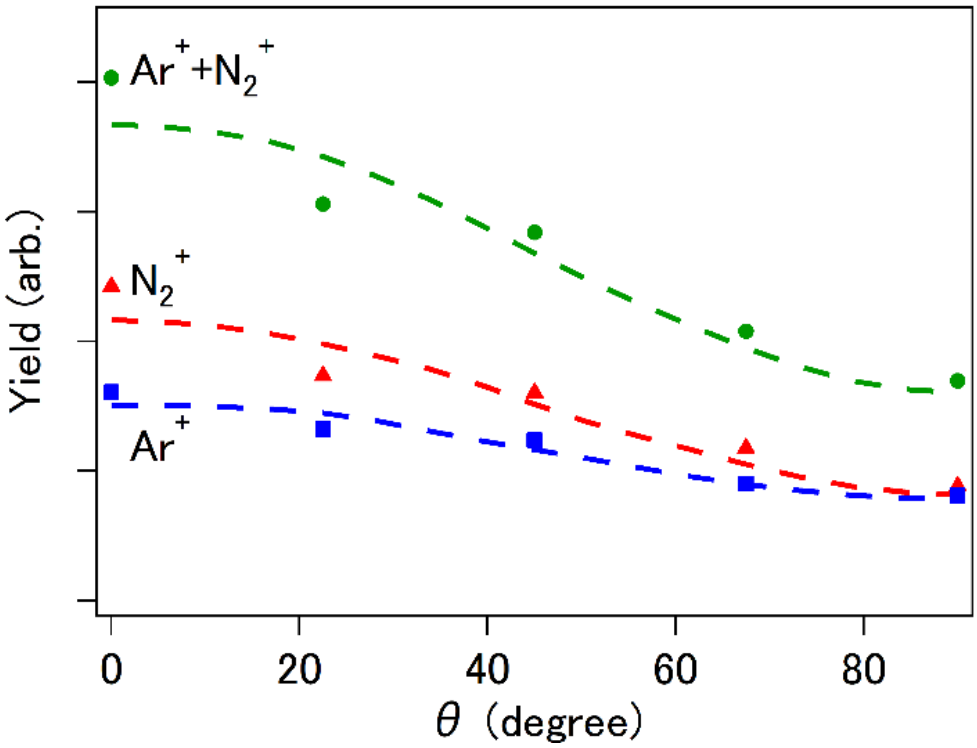

Figure 2.9. The dependences of the yields of Ar^+ (blue squares), N_2^+ (red triangles), and sum of Ar^+ and N_2^+ (green circles) produced by the irradiation of $[Ar\text{-}N_2]^+$ with a femtosecond laser pulse (λ = 800 nm, Δt = 40 fs, I = 3.1×10^{14} W/cm^2) as a function of the angle θ between the laser polarization direction and the TOF axis. The error bars are smaller than the size of the markers

$Ar^+(^2P_{3/2})\cdots N_2(X^1\Sigma^+_g)$ [Ω = 1/2] exhibits a very broad spectrum covering the visible and UV wavelength regions with a very weak tail in the near-IR wavelength region.

References

[1] H. Linnartz and D. Verdes, J. P. Maier, *Science* **297**, 1166 (2002).

[2] H. Verbraal, J. N. P. van Stralen, J. Bouwman, J. S. de Klerk, D. Verdes, H. Linnartz, and F. M. Bickelhaupt, *J. Chem. Phys.* **123**, 144305 (2005).

[3] V. Frecer, D. C. Jain, and A.-M. Sapse, *J. Phys. Chem.* **95**, 9263 (1991).

[4] M. S. B. Munson, F. H. Field, and J. L. Franklin, *J. Chem. Phys.* **37**, 1790 (1962).

[5] H. H. Teng and D. C. Conway, *J. Chem. Phys.* **59**, 2316 (1973).

[6] K. Hiraoka, S. Fujimaki, M. Nasu, A. Minamitsu, S. Yamabe, and H. Kouno, *J. Chem. Phys.* **107**, 2550 (1997).

[7] R. H. Schultz and P. B. Armentrout, *Int. J. Mass Spectrom. Ion Proc.* **107**, 29 (1991).

[8] J. Glosik, V. Skalsky, C. Praxmarer, D. Smith, W. Freysinger, and W. Lindinger, *J. Chem. Phys.* **101**, 3792 (1994).

[9] J. Mähnert, H. Baumgärtel, and K.-M. Weitzel, *J. Chem. Phys.* **102**, 180 (1995).

[10] K.-M. Weitzel and J. Mähnert, *Int. J. Mass Spectrom.* **214**, 175 (2002).

[11] J. H. Langenberg, I. B. Bucur, and P. Archirel, *Chem. Phys.* **221**, 225 (1997).

[12] R. Candori, S. Cavalli, F. Pirani, A. Volpi, D. Cappelletti, P. Tosi, and D. Bassi, *J. Chem. Phys*. **115**, 8888 (2001).

[13] W. Lindinger, F. Howorka, P. Lukac, S. Kuhn, H. Villinger, E. Alge, and H. Ramler, *Phys. Rev. A* **23**, 2319 (1981).

[14] D. Smith and N. G. Adams, *Phys. Rev. A* **23**, 2327 (1981).

[15] M. Hamdan, K. Birkinshaw, and N. D. Twiddy, *Int. J. Mass Spectrom. Ion Processes* **57**, 225 (1984).

[16] C. Rebrion, B. R. Rowe, and J. B. Marquette, *J. Chem. Phys*. **91**, 6142 (1989).

[17] A. A. Viggiano, J. M. Van Doren, R. A. Morris, and J. F. Paulson, *J. Chem. Phys*. **93**, 4761 (1990).

[18] M. Hawley and M. A. Smith, *J. Phys. Chem*. **96**, 6693 (1992).

[19] S. Sato, M. I. Frost, V. E. Bierbaum and S. R. Leone, *Can. J. Chem.* **72**, 625 (1994).

[20] T. Kato, K. Tanaka, and I. Koyano, *J. Chem. Phys*. **77**, 337 (1982).

[21] C.-L. Liao, J.-D. Shao, R. Xu, G. D. Flesch, Y.-G. Li, and C. Y. Ng, *J. Chem. Phys*. **85**, 3874 (1986).

[22] R. H. Schultz and P. B. Armentrout, *Chem. Phys. Lett.* **179**, 429 (1991).

[23] Y. C. Chang, H. Xu, Z. Lu, Y.-H. Chiu, D. L. Levandier, and C. Y. Ng, *J. Chem. Phys.* **134**, 201105 (2011).

[24] Y. C. Chang, Y. Xu, Z. Lu, H. Xu, and C. Y. Ng, *J. Chem. Phys*. **137**, 104202 (2012).

[25] T. R. Govers, P. M. Guyon, T. Baer, K. Cole, H. Fröhlich, and M. Lavollée, *Chem. Phy*s. **87**, 373 (1984).

[26] A. L. Rockwood, S. L. Howard, W.-H. Du, P. Tosi, W. Lindinger, and J. H. Futrell, *Chem. Phys. Lett*. **114**, 486 (1985).

[27] P. M. Guyon, T. R. Gowers, and T. Baer, *Z. Phys. D: At., Mol. Clusters* **4**, 89 (1986).

[28] C.-L. Liao, R. Xu, and C. Y. Ng, *J. Chem. Phys*. **85**, 7136 (1986).

[29] K. Birkinshaw, A. Shukla, S. Howard, and J. H. Futrell, *Chem. Phys*. **113**,149 (1987).

[30] J. H. Futrell, *Int. J. Quantum Chem.* **31**, 133 (1987).

[31] J.-D. Shao, Y.-G. Li, G. D. Flesch, and C. Y. Ng, *J. Chem. Phys.* **86**, 170 (1987).

[32] D. M. Sonnenfroh and S. R. Leone, *J. Chem. Phys*. **90**, 1677 (1989).

[33] P. Tosi, O. Dmitrijev, and D. Bassi, *Chem. Phys. Lett.* **200**, 483 (1992).

[34] M. R. Spalburg, J. Los, and E. A. Gislason, *Chem. Phys.* **94**, 327 (1985).

[35] G. Parlant and E. A. Gislason, *Chem. Phys*. **101**, 227 (1986).

[36] G. Parlant and E. A. Gislason, *J. Chem. Phys*. **86**, 6183 (1987).

[37] G. Parlant and E. A. Gislason, *J. Chem. Phys.* **88**, 1633 (1988).

[38] D. C. Clary and D. M. Sonnenfroh, *J. Chem. Phys*. **90**, 1686 (1989).

[39] R. Candori, F. Pirani, D. Cappelletti, P. Tosi, and D. Bassi, *Int. J. Mass Spec*. **223**, 499 (2003).

[40] H.-S. Kim and M. T. Bowers, *J. Chem. Phys.* **93**, 1158 (1990).

[41] T. F. Magnera and J. Michl, *Chem. Phys. Lett.* **192**, 99 (1992).

[42] M. Halmann and I. Laulicht, *J. Chem. Phys.* **43**, 438 (1965).

[43] K. Kato and K. Yamanouchi, *Chem. Phys. Lett.* **397**, 237 (2004).

[44] T. Yamazaki, Y. Watanabe, R. Kanya, and K. Yamanouchi, *J. Chem. Phys.* **144**, 024313 (2016).

[45] S. Guan and A. G. Marshall, *Int. J. Mass Spectrom*. *Ion Processes* **157/158**, 5 (1996).

[46] A. Kellerbauer, T. Kim, R.B. Moore, and P. Varfalvy, *Nucl. Instrum. Methods Phys. Res. A* **469**, 276 (2001).

[47] W. C. Wiley and I. H. McLaren, *Rev. Sci. Instrum*. **26**, 1150 (1955).

[48] D. A. Dahl, *Int. J. Mass Spectrom*. **200**, 3 (2000).

[49] L. D. Landau, *Phys. Z. Soviet* **2**, 46 (1932).

[50] C. Zener, *Proc. R. Soc. London, Ser. A* **137**, 696 (1932).

[51] E. G. Stückelberg, *Helv. Phys. Acta* **5**, 369 (1932).

[52] V. Aquilanti, R. Candori, F. Pirani, and Ch. Ottinger, *Chem. Phys.* **187**, 183 (1994).

[53] E. Bauer, E. R. Fisher, and F. R. Gilmore, *J. Chem. Phys.* **51**, 4173 (1969).

[54] E. A. Gislason and J. G. Sachs, *J. Chem. Phys.* **62**, 2678 (1975).

[55] E. A. Gislason, G. Parlant, and M. Sizun, *Adv. Chem. Phys.* **82**, 321 (1992).

[56] S. V. Bobashev and V. A. Kharchenko, Electronic and Atomic Collisions, book of abstracts, XVII ICPEAC, edited by I. E. McCarthy, W. R. McGillivray, and M. C. Sandage (IOP Publishing, 1992), p. 664.

[57] T. M. Miller, J. H. Ling, R. P. Saxon, and J. T. Moseley, *Phys. Rev. A* **13**, 2171 (1976).

第 3 章

本章については、 5 年以内に雑誌等で刊行予定のため、非公開。

Chapter 4. Summary and future perspective

Charge transfer in $[Ar\text{-}N_2]^+$ induced by near-IR femtosecond intense laser fields by ion-trap time-of-flight mass spectrometry

By the ion-trap mass spectrometry, I have investigated the photodecomposition processes of $[Ar\text{-}N_2]^+$ ions induced by the irradiation of a 800 nm femtosecond intense laser pulse. The yield ratio of N_2^+ is found to be around 60%, which is significantly larger than the corresponding values reported before when UV and visible light are used for the photodissociation. I have confirmed the yield ratio of N_2^+ fragment ions does not exhibit any significant dependence on laser intensity, laser pulse duration, or laser polarization direction, indicating that the significant enhancement of the N_2^+ yield does not originate from the formation of light-dressed state thorough the highly nonlinear light-molecule interactions induced by intense laser fields. From the numerical simulations of statistical population transfer based on the LZS model, the enhancement of the N_2^+ yield was reproduced when the dissociation via IVR was considered in the simulation. Because the present laser wavelength, 800 nm, is almost resonant with the crossing point between the vibronic curve asymptotically correlating with "$Ar^+(^2P_{3/2}) + N_2(X\ ^1\Sigma_g^+)$ (v = 0)" and that correlating with "$Ar(^1S) + N_2^+(X\ ^2\Sigma_g^+)$ (v' = 6)", the adiabatic population transfer from "$Ar^+(^2P_{3/2}) + N_2(X\ ^1\Sigma_g^+)$ (v = 0)" to "$Ar(^1S) + N_2^+(X\ ^2\Sigma_g^+)$ (v' = 6)" becomes efficient, and consequently, N_2^+ fragment ions are efficiently generated by dissociation into $Ar(^1S) + N_2^+(X\ ^2\Sigma_g^+)$ through the intramolecular vibrational energy redistribution (IVR) processes.

In Chapter 2, only the one photon absorption of $[Ar\text{-}N_2]^+$ ions has been observed, which can be ascribed to the fact that the Franck-Condon overlap is significantly small at 800 nm. Therefore, by adopting the excitation ultrashort-pulsed laser light having the shorter wavelength, it will become possible to investigate nonlinear optical transitions occurring in an intense laser field. By inducing the photodissociation reaction of $[Ar\text{-}N_2]^+$ using intense laser fields, dependences of the yield ratio of the

fragment ions on the laser polarization direction, the laser intensity, and the pulse duration the laser pulse can be investigated, so that the mechanism of the charge transfer processes will be clarified.

Determination of geometrical structure of CCl_3^+ by trapped-ion electron diffraction

I have developed an trapped-ion electron diffraction apparatus. The intensity of the background signals was reduced by two orders of magnitude compared with the previous TIED experiment, and the TIED signals of mass-selective trapped CCl_3^+ ions were recorded for the first time. The optimized internuclear distances obtained by the least-squares analysis of the molecular scattering intensity were determined to be $r_{C\text{-}Cl}$ = 1.66(2) Å and $r_{Cl\text{-}Cl}$ = 2.87(2) Å, which are in good agreement with the previous theoretical values. It was also shown that the obtained temperature of CCl_3^+ ions was as high as 3000 K, suggesting that the relatively large released energy associate with the generation of CCl_3^+ is transferred to the vibrational energy of CCl_3^+ ions.

In order to reduce the uncertainty in the geometrical parameters from the analysis of the recorded $sM(s)$, it is necessary to reduce the background signals, which lower the signal-to-noise ratio of the electron diffraction signals particularly in the range of $s > 11$. The main sources of the background signals are the electrons scattering by residual atoms and molecules and the backscattering and secondary electrons created at the Faraday cap. Therefore, it becomes necessary to separate the ion source from the chamber in which the ion trap is installed, so that the density of the background neutral gas atoms and molecules in the ion trap chamber is sufficiently reduced. It is also necessary to improve the design of the Faraday cup so that the returning backscattering electrons and secondary electrons from the Faraday cup are sufficiently suppressed. Once the signal-to-noise ratio is improved more, the geometrical structure of trapped molecular ions can be determined with high precision and the temporal evolution of the changes in the geometrical structure of trapped ions induced by a fs pump laser pulse can be probed by time-resolved trapped-ion gas electron diffraction measurements.

Acknowledgements

First, I would like to thank my supervisor, Professor Kaoru Yamanouchi, for his thoughtful guidance, deep and extensive discussion, and encouragement throughout the last six years. I also appreciate Professor Reika Kanya for his valuable discussion and advice as well as his experimental assistance. I would like to give thanks to Dr. Takashi Hiroi for his advice and experimental help. I would like to thank also Dr Keiko Kato, Dr. Takao Yamazaki, Mr. Hideaki Tanaka, and Mr. Kazuki Isoyama who developed before the ion trap mass spectrometry and trapped ion electron diffraction apparatus, and Mr. Fumiya Imou who helped me develop the apparatus and measure the experimental data. I express my sincere thanks to all the members of Yamanouchi laboratory for their continuous help and discussion.